Geological Magazine

www.cambridge.org/geo

Original Article

Cite this article: Šegvić B, Slovenec D, and Badurina L (2023) Major and rare earth element mineral chemistry of low-grade assemblages inform dynamics of hydrothermal ocean-floor metamorphism in the Dinaridic Neotethys. *Geological Magazine* **160**: 444–470. https://doi.org/10.1017/S0016756822001030

Received: 19 December 2021
Revised: 23 August 2022
Accepted: 8 September 2022
First published online: 2 November 2022

Keywords:
oceanic crust; hydrothermal metamorphism; low-grade phases; REE mobility; chlorite; Dinaridic Neotethys

Author for correspondence:
Branimir Šegvić,
Email: Branimir.Segvic@ttu.edu

Major and rare earth element mineral chemistry of low-grade assemblages inform dynamics of hydrothermal ocean-floor metamorphism in the Dinaridic Neotethys

Branimir Šegvić[1], Damir Slovenec[2] and Luka Badurina[1]

[1]Texas Tech University, Department of Geosciences, 1200 Memorial Circle, Lubbock TX 79409, USA and [2]Croatian Geological Survey, Sachsova 2, 10000 Zagreb, Croatia

Abstract

This contribution provides insights into ocean-floor hydrothermal metamorphism of the fast-evolving Dinaridic Neotethys. Mineralogical, geochemical and Sr isotope data collected from altered ophiolites and non-ophiolite basalts/andesites and tuffs of the active continental margin are consistent with hydrothermal alteration trajectories that reflect the host-rock composition. This suggests that hydrothermal fluxes were restricted within a simple closed seawater-fed system. Based on the initial isotopic ratios of Sr, two fluid–rock interaction trends are established: (a) low-to-medium degrees of metasomatism in pre-Middle Jurassic anorogenic ophiolites that progressively abated, and (b) increased intensities of metasomatism in post-Middle Jurassic orogenic ophiolites. This agrees with chlorite thermometry and Ca-Al-(Fe)-silicate phase chemistry. The metamorphic assemblages belong to the zeolite, prehnite-pumpellyite, prehnite-actinolite and greenschist facies. The facies is reliant on the temperature of hydrothermal systems and their fluid chemistry. Rare earth element (REE) phase geochemistry shows (a) variable fluid–rock ratios in chlorite and pumpellyite dependent on fluid temperatures, (b) prominent Eu and Ce anomalies that reflect the fluid oxidation state, (c) light REE/heavy REE mobilization attributed to prevalent ligand complexation, and (d) multi-phase fluid percolation across reaction zones of heterogeneous permeability. This study proposes initiation of simple hydrothermal system(s) at or near a spreading centre(s) in the infancy of the Dinaridic Neotethys. Such a system became more complex during Middle Jurassic and Early Cretaceous time with reactive hydrothermal fluids passing the recharge area and reaching the hot reaction zone. An abrupt obliteration of the established high-temperature regime ensued, following the final closure of the Neotethys.

1. Introduction

Hydrothermal metamorphism that takes place in the oceanic lithosphere facilitates our understanding of crustal evolution and offers insights into processes that characterize hydrothermal systems (Alt, 2009; Alt & Teagle, 2000). The hydrothermal interaction of seawater and oceanic crust controls the heat exchange between lithosphere and hydrosphere, which ultimately affects the chemistry of seawater as well as the upper sequences of the oceanic crust. The convective flow of fluids in the crust is governed by the heat released during formation and subsequent cooling of various mafic lithologies (Fyfe & Lonsdale, 1981; Alt & Teagle, 2000; Gillis *et al.* 2005; Wilson *et al.* 2006). Chemical changes taking place in hydrothermal systems have been reported for a broad range of temperatures, pressures and compositions of catalytic fluids at varying seawater/rock ratios (e.g. Mottl, 1983). Mafic extrusive and intrusive rocks of the oceanic crust react with circulating and percolating hydrothermal fluids (i.e. tempered liquid phases), which results in the transformation of primary magmatic minerals into deuteric assemblages. Alternatively, the latter may precipitate directly from the hydrothermal fluid that strongly reflects the geochemistry of affected crystalline rocks. In this contribution, such hydrothermal phases are referred to as 'metamorphic' since hydrothermal metamorphism commonly includes partial recrystallization and the formation of clay minerals; these are essentially out of thermodynamic equilibrium and result in broad compositional ranges (Arbiol *et al.* 2021). These hydrothermal processes are best understood as being metasomatic and allochemical, and prone to the selective addition and removal of chemical components (Harlov & Marschall, 2009; Paoli *et al.* 2019). The hydrothermal metamorphic assemblages may therefore provide information on the alteration setting and post-emplacement alteration processes. Furthermore, over the last few decades research on seawater interaction with mafic and ultramafic rocks has sparked academic interest, which has established a hypothesis on the role of

hydrothermal alteration of mid-ocean-ridge basalts in the global cycling of elements (e.g. Seyfried & Bischoff, 1981; Mottl & McConachy, 1990; German & Lin, 2004; Lowell *et al.* 2013).

In the European Western Vardar ophiolites (in the sense of Schmid *et al.* 2008; Fig. 1), or more precisely in the southwestern segment of the Zagorje-Mid-Transdanubian Zone (ZMTDZ; Pamić & Tomljenović, 1998) or Sava Unit (Haas *et al.* 2000), Mesozoic mafic intrusive, extrusive and pyroclastic rocks crop out in northwestern Croatia (Slovenec *et al.* 2011; Fig. 2). These rocks are incorporated as slices and metre-to-kilometre-sized blocks in ophiolite mélange (Slovenec & Šegvić, 2021) known as the Kalnik Unit (KU) (Haas *et al.* 2000) (Fig. 2). However, the geotectonic affiliation of the KU is still debated; while some argue that it is part of the Western Vardar ophiolites (Fig. 1; e.g. Schmid *et al.* 2008) based on the occurrence of non-ophiolite basalts/andesites and tuffs of the active continental margin (Slovenec & Šegvić, 2021), others suggest that it forms the most southern portion of the Southern Alps (Haas *et al.* 2000; Schmid *et al.* 2008; Fig. 1). The former proposal considers the KU to be an integral part of the Jurassic oceanic accretionary prism (e.g. Schmid *et al.* 2008), while the latter suggests its Middle Triassic continental volcanism to be spatially and genetically related to the onset of the formation of the Tethyan Mesozoic Adriatic-Dinaridic carbonate platform(s) (e.g. Vlahović *et al.* 2005). Such diverse geological histories likely resulted in various hydrothermal assemblages that are dependent on the host lithology, basement architecture, porosity and permeability of the oceanic crust (Alt, 2009).

In this contribution, we provide an overview of the mineralogy as well as the phase and Sr isotope geochemistry of ocean-floor metamorphic parageneses. Compositional variabilities of hydrothermal assemblages were examined in the context of the geological setting of the host rocks (i.e. igneous versus pyroclastic rocks) where particular attention was paid to the rare earth element (REE) mobility during hydrothermal processes, which has long been a matter of concern because of its bearing on the evolution of the oceanic crust (e.g. Michard *et al.* 1983; Michard & Albarède, 1986; Bau, 1991; Klinkhammer *et al.* 1994; Bau & Dulski, 1999). Chlorite and pumpellyite are omnipresent in the oceanic crust preserved in the KU regardless of lithology (Slovenec *et al.* 2012). Acting as either a clay-size replacement of a pyroclastic/effusive matrix and/or a coarse vein infill, chlorite in particular serves as an excellent medium to investigate the mobility of REEs in hydrothermal media controlled by temperature, redox potential, acidity and ionic complexation of pervasive fluids (Brookins, 1989; Tetiker *et al.* 2015). The purpose of this investigation is to (a) find mineralogical and geochemical clues regarding how and to what extent hydrothermal parageneses and their phase chemistry are controlled by the primary lithology, and (b) document the REE distribution in hydrothermal, texturally diverse, chlorite and pumpellyite, in order to test a possible relationship between the REE geochemistry of these minerals and the prevailing hydrothermal conditions.

2. Geological setting

Mesozoic mafic and pyroclastic rocks that crop out at the Intra-Pannonian Inselgebirge of the Sava Unit (Figs 1, 2) are classified as ophiolites and non-ophiolite basalts/andesites and tuffs of the active continental margin. Ophiolites are of Middle–Late Triassic, Jurassic or Cretaceous age and make up an integral part of the subduction-related tectonic mélange of the north Croatian mountains of Kalnik, Ivanščica, Medvednica and Samoborska Gora (Slovenec *et al.* 2011; Lugović *et al.* 2015). These constitute members of the Kalnik Unit (Fig. 2), which represents a chaotic sedimentary/tectonic complex composed of pebbles and slivers, and up to hectometre-to-kilometre-sized blocks of sedimentary and igneous rocks embedded in a pervasively sheared continent-derived Lower–Middle Jurassic pelitic matrix (Fig. 2a–d). According to these authors, the formation of the mélange took place during Middle–Late Jurassic to Early Cretaceous time. This is the period of rapid transition of the Dinaridic branch of Neotethys, which evolved from an active ridge magmatism to an intraoceanic subduction environment and island/back-arc volcanism (Šegvić *et al.* 2014). The sedimentary component of the mélange is made up of Triassic and Jurassic sandstone and chert as well as Lower Cretaceous limestone and clastic rocks. Metre-to-kilometre-sized blocks of magmatic rocks render a fragmented middle-Lower Triassic and Jurassic oceanic crust that constitute upper members of an ophiolite sequence. Those blocks are largely composed of massive and pillow basalts intersected by mafic dikes (Slovenec *et al.* 2011). Tholeiitic cumulate gabbro is a minor lithology (Lugović *et al.* 2015), while alkali basalts and a high-grade metamorphic basement are only locally present (Slovenec *et al.* 2011; Šegvić *et al.* 2016). Five geochemically distinct types of mafic extrusives occur in the magmatic blocks of the KU (Slovenec *et al.* 2011; Lugović *et al.* 2015): (i) within-plate alkaline basalts (WPAB; Middle Triassic, Illirian); (ii) enriched mid-ocean-ridge basalts (E-MORB; Middle Triassic, late Fassanian – early Longobardian); (iii) transitional mid-ocean-ridge basalts (T-MORB; Late Triassic, middle–late Carnian); (iv) very different varieties of essentially normal mid-ocean-ridge basalts (N-MORB; Late Triassic – Midddle Jurassic, latest Carnian–Bajocian); and (v) island-arc basalts (IAT; Middle Jurassic, late Bajocian–Oxfordian). On the other hand, intrusive rocks occur as (i) N-MORB (Early Jurassic, Pliensbachian–Aalenian); (ii) IAT (Middle–Late Jurassic, Callovian–Tithonian); and (iii) back-arc basin basalts (BABB; Early Cretaceous, Albian). Ophiolite rocks are commonly affected by hydrothermal activity, overprinted by metamorphism up to the greenschist facies (Slovenec *et al.* 2012).

Triassic non-ophiolite basalts/andesites and tuffs of the active continental margin emerge as interstratified, hectometre-to-kilometre-sized blocks in volcanosedimentary successions of the north Croatian mountains of Ivanščica, Strahinjščica, Kuna Gora, Desinić Gora, Ravna Gora and Žumberak (Fig. 2). These rocks constitute part of the Southern Alps (Schmid *et al.* 2008; Fig. 1). Volcanic and volcanoclastic rocks are intercalated with Middle Triassic siliciclastic and carbonate marine sediments, and consist of fine-grained and strongly altered basic, intermediate to acid volcanic and pyroclastic lithologies (Marci, 1987; Goričan *et al.* 2005; Slovenec & Šegvić 2021). Alteration processes documented in non-ophiolite basalts/andesites and tuffs are attributed to burial metamorphism and hydrothermal activity, and account for the volcanic glass devitrification, plagioclase degradation and occurrence of low-grade assemblages of prehnite-pumpellyite facies (Marci, 1987). The volcanic activity for that period is represented by submarine andesite to basaltic lava flows accompanied by multiple explosive eruptions of volcaniclastic material. The Middle Triassic volcanosedimentary succession of the Sava Unit can be correlated with the Triassic volcanosedimentary series of the Meliata-Maliak arc-back-arc system (Goričan *et al.* 2005) and analogue successions from the Dinarides (Pamić, 1984; Smirčić *et al.* 2018).

https://doi.org/10.1017/S0016756822001030 Published online by Cambridge University Press

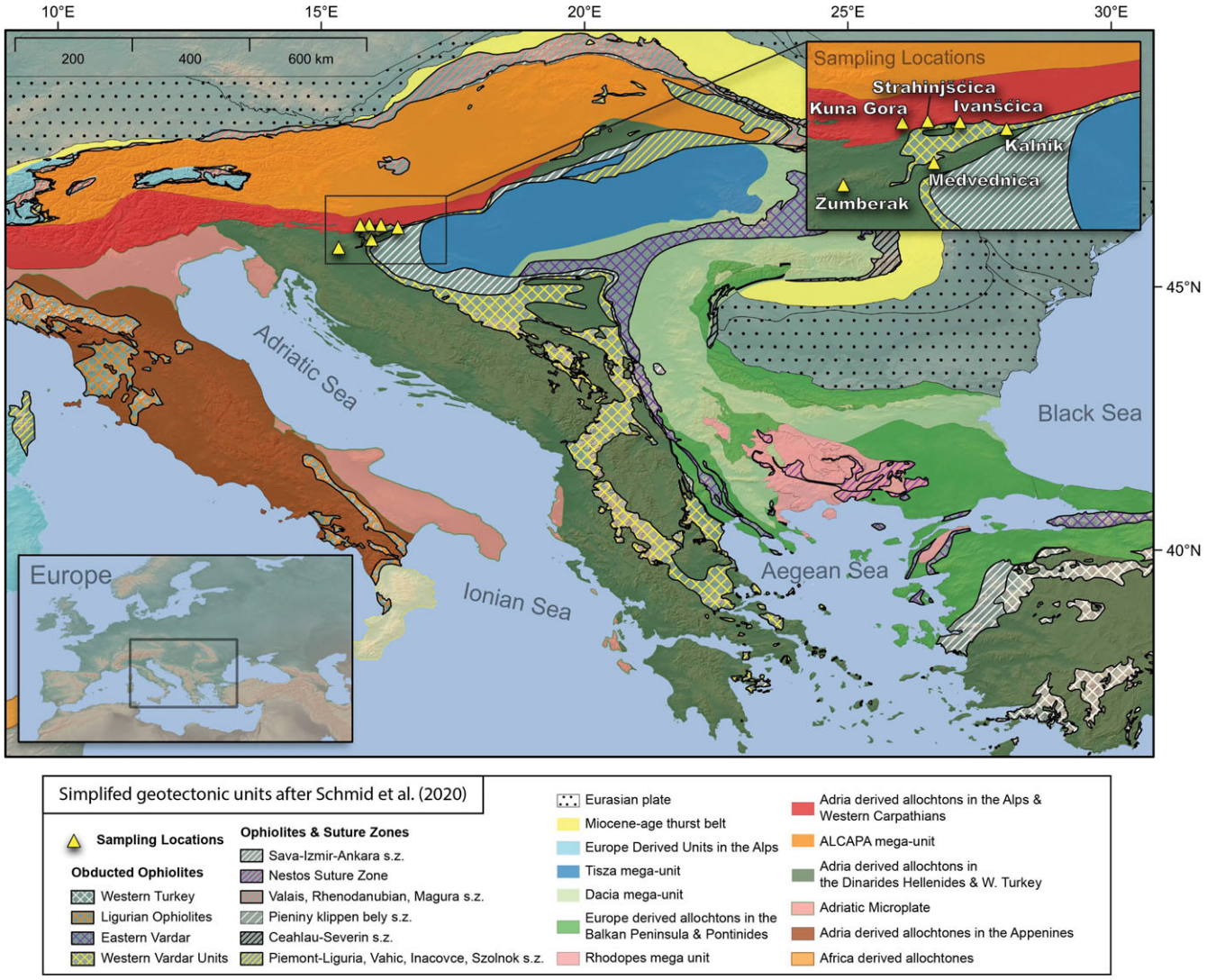

Fig. 1. (Colour online) Simplified geotectonic map showing major units of the Alps, Carpathians and Dinarides (simplified after Schmid *et al.* 2020). The upper inset map shows the research area in more detail.

3. Materials and analytic methods

3.a. Materials

A set of 110 samples of Mesozoic intrusive (gabbro), extrusive (basalt and andesite) and pyroclastic rocks were selected for mineralogical, chemical and Sr isotopic analyses (Table 1). All rock samples were taken from outcrops in the north Croatian mountains of Kalnik, Ivanščica, Strahinjščica, Kuna Gora, Desinić Gora, Ravna Gora, Žumberak, Medvednica and Samoborska Gora (Fig. 2). The ophiolites and non-ophiolite basalts/andesites and tuffs account for 65 and 45 samples, respectively. All samples were first investigated with a petrographic microscope to define the texture of the rocks, as well as primary and secondary mineral assemblages.

3.b. Electron microprobe analyses

Electron microprobe analyses (EMPA) and the elemental X-ray study were carried out at the Institute of Geosciences (Universität Heidelberg, Germany) using a CAMECA SX51 microanalyser equipped with five wavelength-dispersive spectrometers. In total, 39 representative samples were analysed. Measurements were performed using an accelerating voltage of 15 kV, beam current of 20 nA, beam size of *c.* 1 μm (for feldspars, 10 μm) and 10 s counting time for all elements. Natural oxides and silicates were used as standards and for calibration. Raw data were corrected for matrix effects with the PAP algorithm (Pouchou & Pichoir, 1984) provided by CAMECA. Mineral formulas were calculated using the software package MINPET (LR Richard, Gatineau, Québec, Canada).

Two different chlorite geothermometers are utilized in this contribution: the empirical one proposed by Kranidiotis & MacLean (1987) and the semi-empirical one of Inoue *et al.* (2018). The former considers the amount of tetrahedral Al in the structure of Al-rich Mg-Fe chlorite, which is considered to be temperature dependent (details in Arbiol *et al.* 2021). The absolute accuracy of empirical geothermometers has been widely challenged (Arbiol *et al.* 2021); the geothermometer of Kranidiotis & MacLean (1987) has therefore only been used tentatively to show potential differences between the empirical and semi-empirical chlorite thermometers applied in hydrothermal systems. The semi-empirical chlorite geothermometer of Inoue *et al* (2018) is used

https://doi.org/10.1017/S0016756822001030 Published online by Cambridge University Press

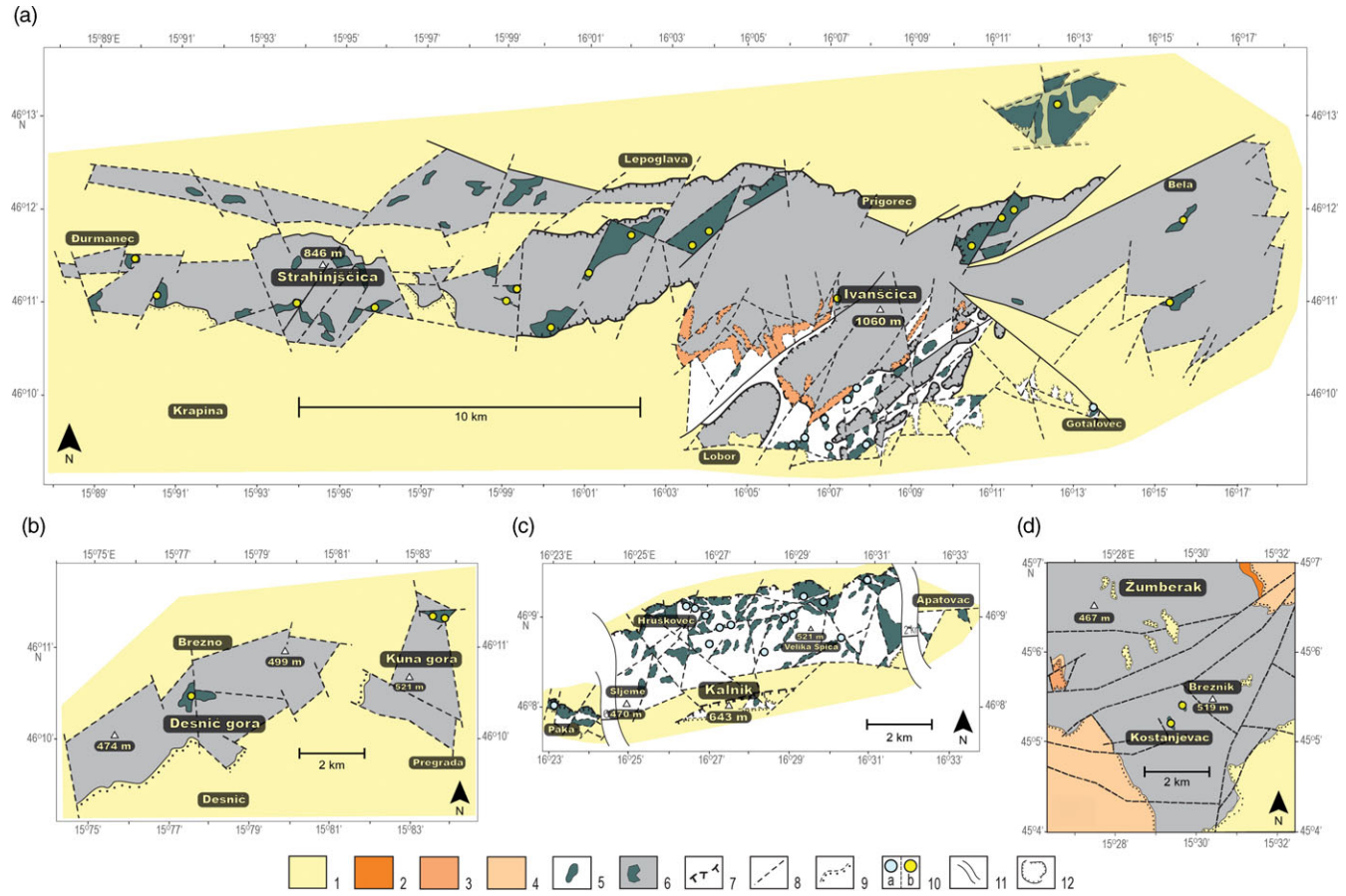

Fig. 2. (Colour online) Simplified geological map of (a) Mounts Ivanščica and Strahinjščica, (b) Mounts Kuna Gora and Desinić Gora, (c) Mount Kalnik and (d) Mount Žumberak (modified after Pletničar *et al.* 1975; Šikić *et al.* 1977; Šimunić *et al.* 1982; Aničić & Jureša, 1984). Legend: 1 – Neogene and Pleistocene sedimentary rocks; 2 – Middle Cretaceous breccias, conglomerates, shales, marls, limestones and cherts; 3 – Upper Jurassic – Lower Cretaceous limestones; 4 – Jurassic limestones, cherts and dolomites; 5 – intercalation of Cretaceous calcarenite, marl and silicified marly limestone, shale and siltite, then ophiolite mélange with blocks of Triassic/Jurassic/Cretaceous basalt, gabbro and tectonite peridotite (green field) and Triassic–Jurassic radiolarites, sandstones and shales (not separated on the maps); 6 – Triassic limestones, dolomites, radiolarites, clastic rocks intersected by a series of andesite-basalts and/or tuffs (green field); 7 – reverse or thrust faults; 8 – normal faults; 9 – discordance line, tectonic-erosion discordance; 10 – sample location (a, ophiolitic rocks; b, non-ophiolitic rocks); 11 – picture break; 12 – quarry.

here because it was initially developed for application to hydrothermal systems and assumes the equilibrium of quartz-chlorite-water. Ideally, the $Fe^{3+}/\Sigma Fe$ should be measured or estimated, as required for the application of most semi-empirical geothermometers; however, the Inoue *et al.* (2018) geothermometer permits the calculation of the formation temperature of chlorite assuming $\Sigma Fe = Fe^{2+}$, which is the approach followed in this contribution.

3.c. Scanning electron microscopy

Scanning electron microscopy (SEM) analyses were completed at the Microscopy Center of Texas Tech University using a Zeiss Crossbeam 540 apparatus equipped with an energy dispersive spectrometer (EDS). Carbon-coated polished thin-sections were utilized for this investigation. The measurements were performed at high vacuum, 15 kV and *c.* 1 nA, with two silicon drift energy dispersive X-ray detectors from Oxford instruments. High-resolution backscatter electron (BSE) images were acquired using a four-quadrant-backscatter detector. The spectra acquisition time was 20 s. Zeiss Aztec software was used for the quantification of EDS spectra in a standardless mode. Chemical data were used as atomic percentages and were normalized to 100%.

3.d. Sr isotope analyses

Strontium isotopic compositions of 38 rocks were measured at the Research Centre for Petrography and Geochemistry (CRPG, Université de Lorraine, France) using a Triton Plus mass spectrometer. Normalizing ratios of $^{86}Sr/^{88}Sr = 0.1194$ were assumed. The $^{87}Sr/^{86}Sr$ ratio for the NBS 987 Sr standard for the period of measurement was 0.710242 ± 0.000030 (2σ). Total procedural blanks were *c.* 500 pg.

3.e. X-ray diffractometry

X-ray powder diffraction (XRD) was carried out on 36 representative samples using a Bruker D8-Advanced diffractometer in the Department of Geosciences at Texas Tech University. The measurements were run using a step scan in the Bragg-Brentano geometry with CuKα radiation. The settings included 45 kV and 40 mA with sample mounts scanned from 3 to 70 °2θ. Measurements were completed under air-dried conditions at a counting time of 2.5 s per 0.02 °2θ. XRD data were processed using a Bruker EVA diffraction suite following recommendations on phyllosilicate interpretation detailed in Arbiol *et al.* (2021).

https://doi.org/10.1017/S0016756822001030 Published online by Cambridge University Press

Table 1. Overview of the studied rock samples from NW Croatian mountains.

Sample	Locality	Rock	Geo-tectonic affinity	Age	Methods	Sample	Locality	Rock	Geo-tectonic affinity	Age	Methods
Non-ophiolite basalts/andesites and tuffs											
tsi-2	IV	BA	CA	Middle Triassic	OM, Sr isotopes	s-112	IV	TU	CA	Middle Triassic	OM, XRD
tsi-4	IV	TU	CA	Middle Triassic	OM	sd-1	IV	BA	CA	Middle Triassic	OM, XRD, LA-ICP-MS
tsi-7	IV	TU	CA	Middle Triassic	OM	j-98	IV	TU	CA	Middle Triassic	OM, XRD
tsi-11	IV	AN	CA	Middle Triassic	OM, XRD	tss-2	ST	AN	CA	Middle Triassic	OM, Sr isotopes
oč-1	IV	BA	CA	Middle Triassic	OM, EPMA	tss-4/2	ST	AN	CA	Middle Triassic	OM, XRD
čo-4a	IV	BA	CA	Middle Triassic	OM, XRD	tss-18	ST	AN	CA	Middle Triassic	OM
čo-11	IV	TU	CA	Middle Triassic	OM, Sr isotopes	tss-25	ST	TU	CA	Middle Triassic	OM
d-4	IV	TU	CA	Middle Triassic	OM, XRD	ce-2	IV	TU	CA	Middle Triassic	OM
d-11	IV	AN	CA	Middle Triassic	OM, Sr isotopes	ce-11	IV	TU	CA	Middle Triassic	OM, Sr isotopes
d-12	IV	AN	CA	Middle Triassic	OM, XRD	ce-16	IV	TU	CA	Middle Triassic	OM, Sr isotopes
d-30	IV	AB	CA	Middle Triassic	OM, XRD, LA-ICP-MS	kšn-2/1	DG	BA	CA	Middle Triassic	OM, XRD
d-50	IV	TU	CA	Middle Triassic	OM, XRD	tskg-1/1	KG	AB	CA	Middle Triassic	OM, XRD
d-54	IV	TU	CA	Middle Triassic	OM, XRD	tskg-1/2b	KG	AB	CA	Middle Triassic	OM, EPMA, Sr isotopes
b-1	IV	BA	CA	Middle Triassic	OM, EPMA	tskg-10	KG	AB	CA	Middle Triassic	OM, Sr isotopes
v-2	IV	BA	CA	Middle Triassic	OM	ta-20	RG	TU	CA	Middle Triassic	OM
v-4	IV	BA	CA	Middle Triassic	OM	ta-20/1	RG	TU	CA	Middle Triassic	OM
v-6	IV	BA	CA	Middle Triassic	OM, XRD, Sr isotopes	kl-14	ŽU	TU	CA	Middle Triassic	OM, XRD
v-91	IV	BA	CA	Middle Triassic	OM	kl-34	ŽU	TU	CA	Middle Triassic	OM
vu-2	IV	AB	CA	Middle Triassic	OM, XRD	kl-40b	ŽU	TU	CA	Middle Triassic	OM, Sr isotopes
bds-1	IV	TU	CA	Middle Triassic	OM, XRD	bz-9	ŽU	TU	CA	Middle Triassic	OM
bd-I/38	IV	TU	CA	Middle Triassic	OM, XRD	bz-26	ŽU	TU	CA	Middle Triassic	OM, XRD
s-14	IV	BA	CA	Middle Triassic	OM, XRD, LA-ICP-MS	bz-32	ŽU	TU	CA	Middle Triassic	OM, XRD, Sr isotopes
vu II-1	IV	BA	CA	Middle Triassic	OM	tskg-1/3d	IV	TU	CA	Middle Triassic	OM, EPMA
Ophiolite rocks											
kb-6	KA	BA	WPAB	Middle Triassic	OM, Sr isotopes	vsk-228	KA	GB	IAT	Middle Jurassic	OM, EPMA
kb-6a	KA	BA	WPAB	Middle Triassic	OM, XRD	vsk-228/2	KA	GB	IAT	Middle Jurassic	OM, Sr isotopes
kb-7	KA	BA	WPAB	Middle Triassic	OM	vsk-217/1	KA	GB	BABB	Early Cretaceous	OM, XRD
vhk-11	KA	BA	WPAB	Middle Triassic	OM, XRD	vsk-229/1	KA	GB	BABB	Early Cretaceous	OM, EPMA, Sr isotopes
h-23	KA	BA	E-MORB	Middle Triassic	OM, XRD	vsk-229/11	KA	GB	BABB	Early Cretaceous	OM

(*Continued*)

Table 1. (*Continued*)

h-33	KA	BA	E-MORB	Middle Triassic	OM, XRD, Sr Isotopes	vsk-229/12	KA	GB	BABB	Early Cretaceous	OM, EPMA
h-33/1	KA	BA	E-MORB	Middle Triassic	OM	be-3	IV	GB	BABB	Early Cretaceous	OM, XRD
vsk-207b	KA	BA	E-MORB	Middle Triassic	OM, XRD, Sr isotopes	vsi-5	IV	GB	BABB	Early Cretaceous	OM, EPMA
ke-2/1	KA	BA	T-MORB	Late Triassic	OM, Sr isotopes	vsi-8/1	IV	GB	BABB	Early Cretaceous	OM, EPMA
ke-15	KA	BA	T-MORB	Late Triassic	OM, XRD	vsi-8/3	IV	GB	BABB	Early Cretaceous	OM, Sr isotopes
vhk-47	KA	BA	T-MORB	Late Triassic	OM, EPMA	gi-2	IV	GB	BABB	Early Cretaceous	OM, Sr isotopes
vhk-236	KA	BA	T-MORB	Late Triassic	OM	gtc-3	IV	GB	BABB	Early Cretaceous	OM, EPMA
ja-2/2	KA	BA	N-MORB	Late Triassic – Middle Jurassic	OM, Sr isotopes	gtc-5	IV	GB	BABB	Early Cretaceous	OM, EPMA
vhk-15	KA	BA	N-MORB	Late Triassic – Middle Jurassic	OM, EPMA	sb-5	ME	BA	WPAB	Middle Triassic	OM
vsk-215/4	KA	BA	N-MORB	Late Triassic – Middle Jurassic	OM, EPMA	sb-9	ME	BA	WPAB	Middle Triassic	OM, EPMA, Sr isotopes
vsk-221	KA	BA	N-MORB	Late Triassic – Middle Jurassic	OM, EPMA	vh-1001/1	ME	BA	WPAB	Middle Triassic	OM, Sr isotopes
vsi-1	IV	BA	N-MORB	Late Triassic – Middle Jurassic	OM	vs-113/3	ME	BA	WPAB	Middle Triassic	OM, Sr isotopes
vsi-6/5	IV	BA	N-MORB	Late Triassic – Middle Jurassic	OM, EPMA, Sr isotopes	t-51/1	ME	BA	N-MORB	Late Triassic – Middle Jurassic	OM, Sr isotopes
ib-2	IV	BA	N-MORB	Late Triassic – Middle Jurassic	OM, XRD	vs-420	ME	BA	N-MORB	Late Triassic – Middle Jurassic	OM
h-26	KA	BA	IAT	Middle Jurassic	OM, Sr Isotopes	vs-486	ME	DI	N-MORB	Late Triassic – Middle Jurassic	OM, XRD, EPMA, Sr isotopes
vsk-18	KA	BA	IAT	Middle Jurassic	OM	kv-1	ME	DI	N-MORB	Late Triassic – Middle Jurassic	OM
vsi-12	IV	BA	IAT	Middle Jurassic	OM	vs-328	ME	BA	N-MORB	Late Triassic – Middle Jurassic	OM, Sr isotopes
vsi-6/1	IV	BA	IAT	Middle Jurassic	OM, EPMA	m-17	ME	BA	IAT	Middle Jurassic	OM, Sr isotopes
vsi-8/4	IV	BA	IAT	Middle Jurassic	OM	m-18/1	ME	BO	IAT	Middle Jurassic	OM, Sr isotopes
vsi-9	IV	BA	IAT	Middle Jurassic	OM, EPMA	vh-49/3	ME	BO	IAT	Middle Jurassic	OM, Sr isotopes
got-6	IV	BA	IAT	Middle Jurassic	OM, XRD	mc-2	ME	GB	IAT	Middle Jurassic	OM, Sr isotopes
got-6/1	IV	BA	IAT	Middle Jurassic	OM, Sr isotopes	vs-386	ME	GB	IAT	Middle Jurassic	OM
gtc-1	KA	BA	IAT	Middle Jurassic	OM, EPMA	rn-13	ME	GB	IAT	Middle Jurassic	OM
gtc-2	KA	BA	IAT	Middle Jurassic	OM, EPMA	jf-33/2	SG	BA	N-MORB	Late Triassic – Middle Jurassic	OM, XRD

(*Continued*)

Table 1. (*Continued*)

Sample	Locality	Rock	Geo-tectonic affinity	Age	Methods	Sample	Locality	Rock	Geo-tectonic affinity	Age	Methods
g-6	KA	BA	IAT	Middle Jurassic	OM, EPMA	jf-34/1	SG	BA	N-MORB	Late Triassic – Middle Jurassic	OM, Sr isotopes
vsk-242	KA	GB	N-MORB	Late Triassic – Middle Jurassic	OM, Sr isotopes	t-23b/1	SG	BA	N-MORB	Late Triassic – Middle Jurassic	OM, EPMA, Sr isotopes
vsk-242/2	KA	GB	N-MORB	Late Triassic – Middle Jurassic	OM, EPMA	sat-210	SG	BA	WPAB	Middle Triassic	OM, EPMA
vsk-242/4	KA	GB	N-MORB	Late Triassic – Middle Jurassic	OM	92-16	SG	BA	WPAB	Middle Triassic	OM, Sr isotopes

AN – andesite; AB – andesite-basalt; BA – basalt; BABB – back-arc basin basalts; BO – boninite; CA – calc-alkaline; DG – Desinić Gora Mount; DI – diabase; E-MORB – enriched mid-ocean-ridge basalts; EMPA – electron microprobe analyses; GB – gabbro; IAT – island-arc tholeiites; IV – Ivanščica Mount; KA – Kalnik Mount; KG – Kuna Gora Mount; LA-ICP-MS – laser ablation inductively coupled plasma mass spectrometry; ME – Medvednica Mount; N-MORB – normal mid-ocean-ridge basalts; OM – optical microscopy; RG – Ravna Gora Mount; SG – Samoborska Gora Mount; ST – Strahinjščica; T-MORB – transitional mid-ocean ridge basalts; TU – tuff (andesite/dacite/rhyolite); WPAB – within-plate alkaline basalts; XRD – X-ray diffraction; ŽU – Žumberak Mount.

3.f. Laser ablation – inductively coupled plasma – mass spectrometry

The REE content of chlorite and pumpellyite was measured in three polished thin-sections of representative basaltic rocks using an Agilent 7500cs quadrupole mass spectrometer coupled with a New Wave UP-213 solid-state laser with dual-volume cell installed at the Geoanalytical Laboratory of Texas Tech University. For each sample, three to five measurements of phases of interest were undertaken. Individual measurements typically comprised 30-s-long background measurements followed by 20- to 40-s-long acquisitions with the activated laser. The choice of measurement spot locations was facilitated using a BSE image from the SEM. The laser was operated using a frequency of 15 Hz, a spot size of 40 μm and a measured fluence of 6–7 J cm^{-2}. For every measurement, corresponding time-resolved charts displaying counts-per-second (cps) data were examined for potential mineral contaminations. The GSD-1 Universal Geotechnical Standard and Si abundances from EDS microanalyses were used as external and internal standards, respectively. The United States Geological Survey rock standard BHVO-2 served to monitor instrument performance, precision and accuracy (Jochum *et al.* 2005).

4. Results

4.a. Light microscope petrography

Petrographic studies of intrusive, effusive and pyroclastic rocks have previously been conducted (e.g. Slovenec *et al.* 2011; Slovenec & Šegvić, 2021) and, as a result, only the most pertinent information is provided here. Intrusive rocks from the KU ophiolite mélange are represented by cumulate and non-cumulate medium- to coarse-grained gabbro that shows a preserved igneous fabric and heteroadcumulate poikilitic, and/or anhedral granular texture and homogenous structure (Fig. 3a–c). The crystallization sequence of cumulate gabbro commenced with olivine, clinopyroxene (augite and diopside) and plagioclase (bytownite and anorthite), whereas amphibole (tschermakite, edenite and magnesiohornblende) and Fe-Ti oxide (magnetite-ulvöspinel) are late-stage crystallization products. The gabbro consists of plagioclase, augite and Fe-Ti oxide (Fig. 3b, c). Gabbroic rocks of the KU mélange bear an omnipresent prehnite-pumpellyite to greenschist facies metamorphic overprint that produced hydrothermal assemblages consisting of albite, tremolite/actinolite, chlorite, serpentine, prehnite, pumpellyite, titanite and muscovite (Fig. 3b, c).

Extrusive rocks of the KU ophiolite mélange consist of basaltic pillow lavas and massive lavas (Fig. 3d–g). Petrographic evidence suggests the following crystallization order: ± spinel (ulvöspinel-magnetite, chromite) → plagioclase (andesine to labradorite) → clinopyroxene (augite) + plagioclase (andesine to labradorite) ± Fe-Ti oxides (ilmenite). However, in the IAT-type lavas, plagioclase phenocrysts may enclose clinopyroxene indicating a somewhat different crystallization order: ± spinel (ulvöspinel-magnetite, chromite) → clinopyroxene (augite) → plagioclase (andesine to labradorite) ± Fe-Ti oxides (ilmenite). The primary assemblages are commonly altered to albite or peristerite, illite/mica, saussurite, calcite, chlorite, zoisite, epidote, leucoxene, analcime, prehnite, pumpellyite, quartz and zeolite (Fig. 3d–f), indicating the ocean-floor hydrothermal overprint in the zeolite – prehnite-pumpellyite – lower greenschist facies (Mével, 2003).

Non-ophiolite Middle Triassic basalts/andesites and tuffs derived from an active continental margin are interstratified in volcanosedimentary successions of the north Croatian mountains

https://doi.org/10.1017/S0016756822001030 Published online by Cambridge University Press

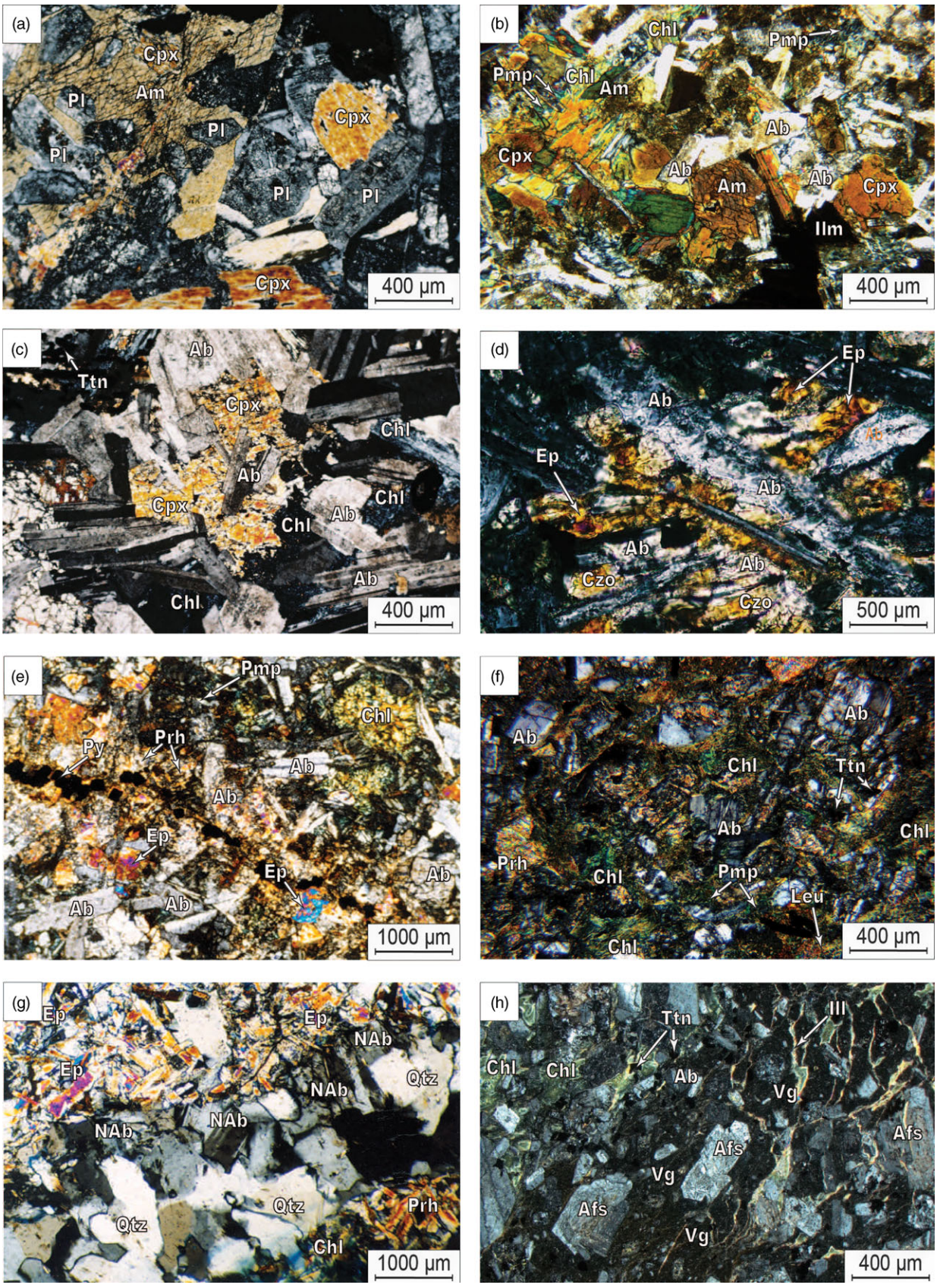

Fig. 3. (Colour online) Microphotographs of gabbros: (a) sample mc-2, N+; (b) sample vsk-228, N+; (c) sample be-3, N+ and basalts; (d) sample vsk-215/4, N+; (e) sample vk-372, N+; (f) sample got-6, N+; (g) sample vs-220, N+ from Mounts Kalnik, Ivanščica and Medvednica ophiolite mélange and andesite-basalt; (h) sample tskg-1/2b N+ from Mount Kuna Gora. Legend: Ab – albite; Afs – alkali feldspar; Am – amphibole; Chl – chlorite; Cpx – clinopyroxene (augite); Ep – epidote; Ill – illite; Ilm – ilmenite; Leu – leucoxene; NAb – neoalbite; Pl – plagioclase; Pmp – pumpellyite; Prh – prehnite; Py – pirite; Qtz – quartz; Ttn – titanite; Vg – volcanic glass.

https://doi.org/10.1017/S0016756822001030 Published online by Cambridge University Press

(Figs 1, 2). These rocks include massive basic, intermediate to acid lavas and spatially associated fine-grained, pyroclastic rocks (i.e. tuffs). Volcanic rocks are characterized by ophitic through porphyritic and glomeroporphyritic seriate textures, which may gradually change to a fluidal texture (Fig. 3h). On the other hand, pyroclastic rocks show vitroclastic, vitro-crystalloclastic, litho-crystalloclastic and vitro-litho-crystalloclastic ash flow tuffs (i.e. ignimbrite) of crystallo-vitrophyre structure and fluidal texture. The volcanic rock microcrystalline matrix is holocrystalline to hypocrystalline and consists of devitrified volcanic glass and microlites of plagioclase/albite and K-feldspar with some minor Fe-Mg phases (Fig. 3h). The primary crystallization sequence is K-feldspar (sanidine) ± plagioclase (bytownite to anorthite) ± clinopyroxene (augite) ± amphibole ± Fe-Ti oxides (ilmenite, magnetite).

Accessory phases are zircon, apatite, rutile, haematite, pyrite, chalcopyrite and illite. The primary assemblage is commonly altered to illite/mica, albite, chlorite, calcite, leucoxene, quartz, and various clay minerals (Fig. 3h), while the glassy matrix altered into a mixture of fine-grained chlorite and mica whose occurrence is indicative of hydrothermal metamorphism (e.g. Tillick *et al.* 2001; Wang *et al.* 2018; Arbiol *et al.* 2021). Conversely, the presence of clay-mineral-rich assemblages calls for somewhat lower temperatures that correspond to diagenetic and very low-grade metamorphic conditions (Alt, 2009; Šegvić *et al.* 2020).

4.b. XRD mineralogy and EMPA chemistry of hydrothermal phases

The distribution and relative abundances of hydrothermal and weathering secondary phases in analysed ophiolite and non-ophiolite basalts/andesites and tuffs are provided in Table 2, while representative phase chemistry and calculated mineral formulas are given in online Supplementary Tables S1a–e (available at http://journals.cambridge.org/geo). Alteration minerals comprise about two-thirds of the studied rocks. The most abundant alteration products are albite, chlorite and quartz. Minor hydrothermal phases are amphibole, pumpellyite, zeolite, prehnite, epidote/clinozoisite, titanite, rutile, illite/mica, kaolinite, calcite, Fe-oxides, sulphides, carbonates, serpentine-phases, sepiolite/palygorskite, stilpnomelane and various expandable clay minerals. In comparison to ophiolite rocks, the non-ophiolite basalts/andesites and tuffs show notable differences in their hydrothermal mineralogy, which contain more quartz, calcite, illite/mica, illite-smectite and pumpellyite. Conversely, these rocks seem to be comparatively impoverished in titanite, rutile, ilmenite and epidote.

4.b.1. Amphibole

Amphibole occurs in N-MORB (Early Jurassic, Pliensbachian–Aalenian), IAT (Middle–Late Jurassic, Callovian–Tithonian) and BABB (Early Cretaceous, Albian) isotropic and cumulate gabbro and gabbrodiorite from the KU mélange (Table 2; online Supplementary Table S1a). It largely consists of brown subhedral pleochroic magnesiohornblende (up to 2 mm) and anhedral pale green tremolite (Figs 3a, b, 4a–f, 5a). Rare fibres of Fe-anthophyllite marked by a faint pleochroism and minute size (< 0.02 mm) also occur (Figs 4d, 5b).

In general, hydrothermal amphibole is characterized by a narrow range of Al_2O_3 (< 3.54 wt%; $Al^{IV} = 0.122–0.537$ apfu), high FeO (17.00–34.82 wt%) and relatively low Mg no. (27.7–58.0; the lowest being in anthophyllite), as well as low total alkalis (Na+K < 0.5 apfu) and Ti (≤ 0.136 apfu) (Fig. 5c). Compared with tremolite, magnesiohornblende has a higher content of Cr_2O_3 and TiO_2, while TiO_2 and K_2O abundances are the lowest in anthophyllite (Table 2; online Supplementary Table S1a).

4.b.2. Epidote

Epidote occurs only in IAT (Lower Jurassic) isotropic gabbro and BABB (Upper Jurassic – Lower Cretaceous) gabbrodiorite (Fig. 4a). Rarely, it occurs in N-MORB (Late Triassic – Middle Jurassic) and IAT (Late Jurassic) basalts from the KU ophiolite mélange (Table 2; online Supplementary Table S1a; Figs 3d, e, 6d). Epidote has constant concentrations of Fe^{3+} (0.880–0.944 apfu), Al^{VI} (2.050–2.198 apfu) and Ca (1.882–1.952 apfu). The Mn-content of epidote is low (0.012–0.014 apfu) and is coupled with high concentrations of Fe^{3+} (Fig. 7a). In gabbro, xenomorphic epidote is accompanied by prehnite and chlorite to fill rare millimetre-sized cross-cutting veins.

4.b.3. Feldspars

In ophiolites, hydrothermal albite (Table 2) is largely a product of a complete alteration of plagioclase ($An_{73.9-15.5}Ab_{82.9-26.1}Or_{1.6-0.1}$) (Figs 4, 6), while in non-ophiolite andesite and basalts it grows on a substrate consisting of K-feldspar (Fig. 3h). In albite, the contents of SiO_2, Al_2O_3 and FeO vary within a narrow range with the An content spanning 0.69–9.52 (online Supplementary Table S1c; Fig. 7b). Fine-grained muscovite as well as the mineral aggregate saussurite are commonly associated with albite in the form of hydrothermal alteration products of igneous plagioclase. The latter is especially common in Jurassic rocks rich in chlorite.

4.b.4. Chlorite

Chlorite is a common hydrothermal alteration phase in all rock types, and is the most abundant secondary mineral after albite (Table 2; Figs 3b–h, 4, 6). Chlorite is characterized by a narrow range of SiO_2 and Al_2O_3 contents, which are the lowest in the youngest (Lower Cretaceous) BABB gabbroic rocks (online Supplementary Table S1b). As per octahedral layer cation occupancy (5.49–6.33 apfu), chlorite is tri-octahedral (Type 1, Fig. 7c). The nature of dominant divalent cation (i.e. clinochlore versus chamosite) was found to reflect the geotectonic affiliation of host rocks; namely, the ratio of Fe^{2+}/Mg steadily increased starting with the WPAB (Middle Triassic, Illirian), through E-MORB (Middle Triassic, upper Fassanian – lower Longobardian), T-MORB (Upper Triassic, middle–upper Carnian), N-MORB (Upper Triassic, upper Carnian – middle Norian; Middle Jurassic, Bajocian), IAT (Middle Jurassic, upper Bajocian – Oxfordian; Upper Jurassic, Callovian–Tithonian) to BABB (Lower Cretaceous, Albian) gabbro and/or basalt (Fig. 7c, d).

Radial to fibrous chlorite commonly occurs in the interstices of pyroxene and plagioclase (Fig. 3b, e, f). In ophiolitic rocks, chlorite is accompanied by epidote, prehnite, calcite and neoalbite (Fig. 3g). Where associated with pumpellyite, it commonly occurs on the peripheral parts of basaltic pillows. In non-ophiolite basalts/andesites and tuffs, however, fine-layered chlorite is a product of devitrification of weathered volcanic glass (Fig. 3h). Chlorite in those rocks commonly forms a substrate of the hypocrystalline matrix or fills monomineralic amygdules (online Supplementary Fig. S1a, b); alternatively, it may be associated with vein carbonates (online Supplementary Table S1b). The matrix is a mixture of *c.* 10-μm-sized Mg-chlorite and altered feldspar. Numerous, 0.1–2-mm-long elliptical to circular amygdules filled with Mg-chlorite dominate the matrix (online Supplementary Fig. S1b). The contact of amygdaloidal chlorite and rock matrix is sharp, but with a visible 1–5-μm-thick reaction front (online

https://doi.org/10.1017/S0016756822001030 Published online by Cambridge University Press

Table 2. Distribution and XRD/EMPA relative abundances of hydrothermal alteration phases in the studied Mesozoic ophiolite and non-ophiolite basalts/andesites and tuffs.

Sample	Rock/ Affiliation	Am	Ep	Czo	Chl	Ab	Prh	Pmp	Zeo	Ttn	Rt/ Ant	Ap	Ilm	Sme	I-S	I/M	Kln	Cal	Hm/ Mt	Py/ Hpy/ Po	Qtz	Hall	Dol	C-S	Ver	Sep/ Pal	Liz	Stp
Non-ophiolite rocks																												
bd-I/38	TU/CAB	–	–	–	+	–	–	–	–	–	–	–	–	–	–	+	++	++	–	+	++	*	–					
bd-IV/1	TU/CAB	+			++	++	+								+	+					++		+					
bds-1	TU/CAB				+	++										++		+			++			+				
bz-26	TU/CAB														+	+		++			++							
bz-32	TU/CAB					+										+	+	++		*	++							
čo-4A	BA/CAB	*														++		++	+									
d-4	TU/CAB										+	+			+	++		++			++							
d-12	AN/CAB	*				++		+							*	++			+									
d-30	AB/CAB	*			++	++		++								+												
d-50	TU/CAB	+				++			++							+					+							
d-54	TU/CAB	*	+		++	++										++												
j-98	TU/CAB				+	++										+	*	++			++							
kl-14	TU/ CAB				+										+	+					++		++					
kl-40a	TU/ CAB								+					+	+	+					++							
kšn-2/1	BA/CAB				+	++										+	*							++				
s-14	BA/CAB	*	+		++	++		++								+					++							
s-112	TU/CAB				++										+	++			+		++							
sd1	BA/CAB	*			++	++										+		++			++							
tsi-4	TU/CAB	*			++	++	+								+	+		++			++							
tskg-1/ 1	AB/CAB				++											+			+		++							
tskg-1/ 2b	AB/CAB				x	x					x								x									
tskg-1/ 3d	TU/CAB				x	x																						
tsi-11	AN/CAB	+				++							+		+	*					+		+					
tss-4/2	AN/CAB	*			++	++									*	+		++	+		++							
v-6	BA/CAB	*			++	++		+								+		+			++							
vu-91	BA/CAB	+			++	++		+								++					++							
vu-2	AB/CAB	+			++	++	+									+		++	+									

(*Continued*)

Table 2. (*Continued*)

Sample	Rock/ Affiliation	Am	Ep	Czo	Chl	Ab	Prh	Pmp	Zeo	Ttn	Rt/ Ant	Ap	Ilm	Sme	I-S	I/M	Kln	Cal	Hm/ Mt	Py/ Hpy/ Po	Qtz	Hall	Dol	C-S	Ver	Sep/ Pal	Liz	Stp
vu II-1	BA/CAB				x	x	–	x																				
oč-1	BA/CAB			x	x	x		x		x								x										
b-1	BA/CAB				x	x							x							x								
Ophiolite rocks																												
kb-6a	BA/WPAB	*	*		++	++		+	+	+		+				+		++			+			+				
vhk-11	BA/WPAB				++	++				+						+		+	+		+			*				
sb-9	BA/WPAB				x	x	x	x		x																		
sat-210	BA/WPAB				x	x					x							x			x							
h-23	BA/E-MORB	*			++	++		+	+	+	+							++	+	*				*				
h-33	BA/E-MORB	*			++	++		+	+							+		++		+				+			*	
vsk-207/b	BA/E-MORB				+	+																						
ke-15	BA/T-MORB	*			+	++			+	+								++						+	+		+	
vhk-47	BA/T-MORB				x	x	x	x		x																		
vsk-215/4	BA/N-MORB		x		x	x	x	x		x											x							
vsk-221	BA/N-MORB				x	x	x																					
t-23b/1	BA/N-MORB				x	x										x												
vhk-15	BA/N-MORB				x					x			x							x								
vsi-6/5	BA/N-MORB				x					x									x									
pu-2	BA/N-MORB				x	x				x	x																	
vs-486	DI/N-MORB	+	x		++	++	+	+	+	+	+					+		+	+	+	++			+				
ib-2	BA/N-MORB				++	++				*									*					+		*		
jf-33/2	BA/N-MORB	*	*		+	++								+		+			+					+			+	

(*Continued*)

Table 2. (*Continued*)

vsk-242/2	GB/N-MORB	x			x	x	x					x																		
vsi-9	BA/IAT				x	x		x		x									x	x										
Ophiolite rocks																														
vsi-6/1	BA/IAT				x	x		x		x										x										
got-6	BA/IAT	*			++	++	+	+		x										+					+	*		+		
gtc-1	BA/IAT		x		x	x				x			x																	
gtc-2	BA/IAT				x	x				x																				
g-6	BA/IAT	x				x				x			x																	x
vsk-228	GB/IAT	x	x		x	x				x	x	x	x						x											
vs-386	GB/IAT	x			x	x		x								x														
be-3	GB/BABB	+			*	++					+		+	+						*						*	+	+		
vsk-217/1	GB/BABB	*			+	++	+			+	+		+							*		+				*				
vsk-229/1	GB/BABB	x			x	x	x			x	x	x	x								x									
vsk-229/12a	GB/BABB				x	x	x			x	x		x																	
vsi-5	GB/BABB	x			x	x				x	x		x																	
vsi-8/1	GB/BABB				x	x		x			x	x	x						x											
gtc-3	GB/BABB	x	x		x	x				x	x		x			x						x								x
gtc-5	GB/BABB	x			x	x		x		x	x		x			x														x

Ab – albite; AB – andesite-basalt; Am – amphibole; AN – andesite; Ant – anatase; Ap – apatite; BA – basalt; BABB – back-arc basin basalts; CAB – calc-alkaline basalts; Cal – calcite; Chl – chlorite; C-S – chlorite-smectite; Czo – clinozoisite; DI – diabase; Dol – dolomite; E-MORB – enriched mid-ocean-ridge basalts; Ep – epidote; GB – gabbro; Hal – halloysite; Hm – haematite; Hpy – chalcopyrite; IAT – island-arc tholeiites, Ilm – ilmenite; I/M – illite/mica; I-S – illite-smectite; Kln – kaolinite; Liz - lizardite; Mt – magnetite; N-MORB – normal mid-ocean-ridge basalts; Pal – palygorskite; Pmp – pumpellyite; Po – pyrrhotite; Prh – prehnite; Py – pyrite; Qtz – quartz; Rt – rutile; Sep – sepiolite; Sme – smectite; Stp – stilpnomelane; T-MORB – transitional mid-ocean-ridge basalts; Ttn – titanite; TU – tuff; Ver – vermiculite; WPAB – within-plate alkaline basalts; Zeo – zeolite; ++ – major phases; + – minor phases; * – phases present, but not unequivocally confirmed by XRD; x – phases detected by EMPA in samples not measured by XRD. Mineral abbreviations after Kretz (1983).

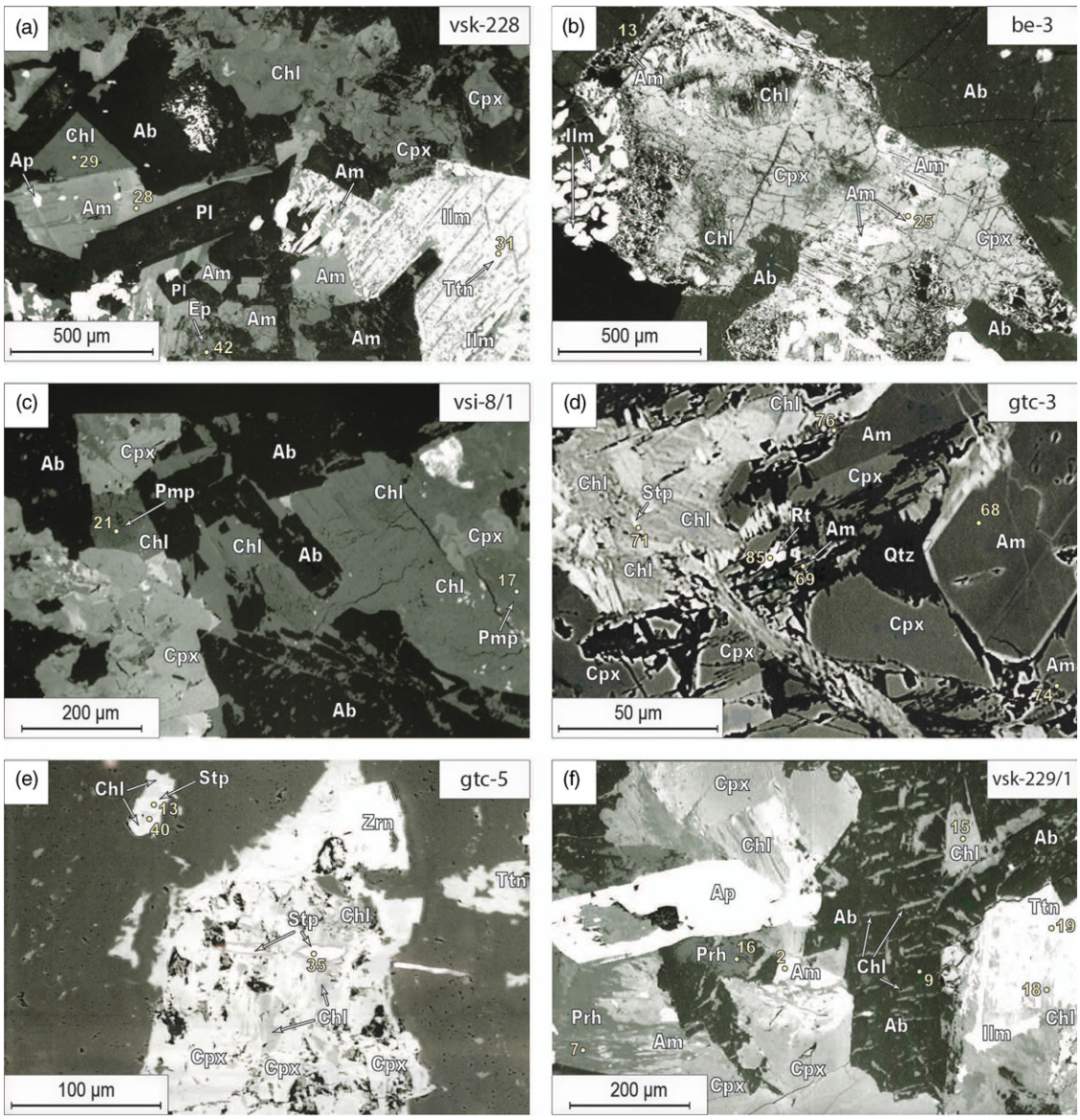

Fig. 4. (Colour online) BSE microphotographs of gabbros: (a) sample vsk-228; (b) sample be-3; (c) sample vsi-8/1; (d) sample gtc-3; (e) sample gtc-5; (f) sample vsk-229/1 from Mounts Kalnik and Ivanščica ophiolite mélange. Numbered acquisition points correspond to the data in online Supplementary Tables S1a–S1e. Legend: Ab – albite; Am – amphibole; Ap – apatite; Chl – chlorite; Cpx – clinopyroxene (augite); Ep – epidote; Ilm – ilmenite; Pmp – pumpellyite; Prh – prehnite; Qtz – quartz; Rt – rutile; Stp – stilpnomelane; Ttn – titanite; Zrn – zircon.

Supplementary Fig. S1b). Amygdaloidal as well as matrix chlorite likely formed concomitantly with intensive albitization (Fig. 6e) and sericitization. Carbonate veins commonly cross-cut chlorite amygdules as well as the matrix (online Supplementary Fig. S1a), thus marking the youngest alteration event. These veins are made of Fe-dolomite, graphite and kaolin minerals, as well as inclusions of the matrix of the host rocks.

The empirical and semi-empirical geothermometers of Kranidiotis & MacLean (1987) and Inoue *et al.* (2018) were applied to the compositions of chlorite. For that purpose, two broadly defined textural types of chlorite were identified (interstitial and vein). The former occurs in the interstices of pyroxene and plagioclase/albite or as their alteration product (Figs. 3b, e, f), while the latter fills circular amygdules and is present in microveins in the hypocrystalline matrix of various rock types (Fig. 6e). The geothermometer of Inoue *et al.* (2018) yields two distinct populations that are related to chlorite microtexture; interstitial chlorite shows temperatures of 92–489 °C (mostly 112 and 251 °C) and vein chlorite yields temperatures of 72–100 °C (online Supplementary Fig. S2). Geothermometric calculations using the Kranidiotis & MacLean (1987) geothermometer returned comparable formation temperatures for vein chlorite, whereas calculated temperatures of interstitial chlorite are *c.* 50–100 °C lower than those yielded by the geothermometer of Inoue *et al.* (2018). Accordingly, we rely on the temperatures of Inoue *et al.* (2018) because the empirical geothermometer of Kranidiotis & MacLean (1987) gives unrealistically low temperatures (online Supplementary Fig. S2).

4.b.5. Prehnite

Prehnite occurs in ophiolites as well as in most of the Middle Triassic non-ophiolite basalts (Table 2). However, its abundance is rather modest except in cumulate gabbro and pillow lavas where it is commonly associated with pumpellyite (Figs 3e, f, 6c–e). Prehnite occurs as needle- to plate-like aggregates (Fig. 3e). The

https://doi.org/10.1017/S0016756822001030 Published online by Cambridge University Press

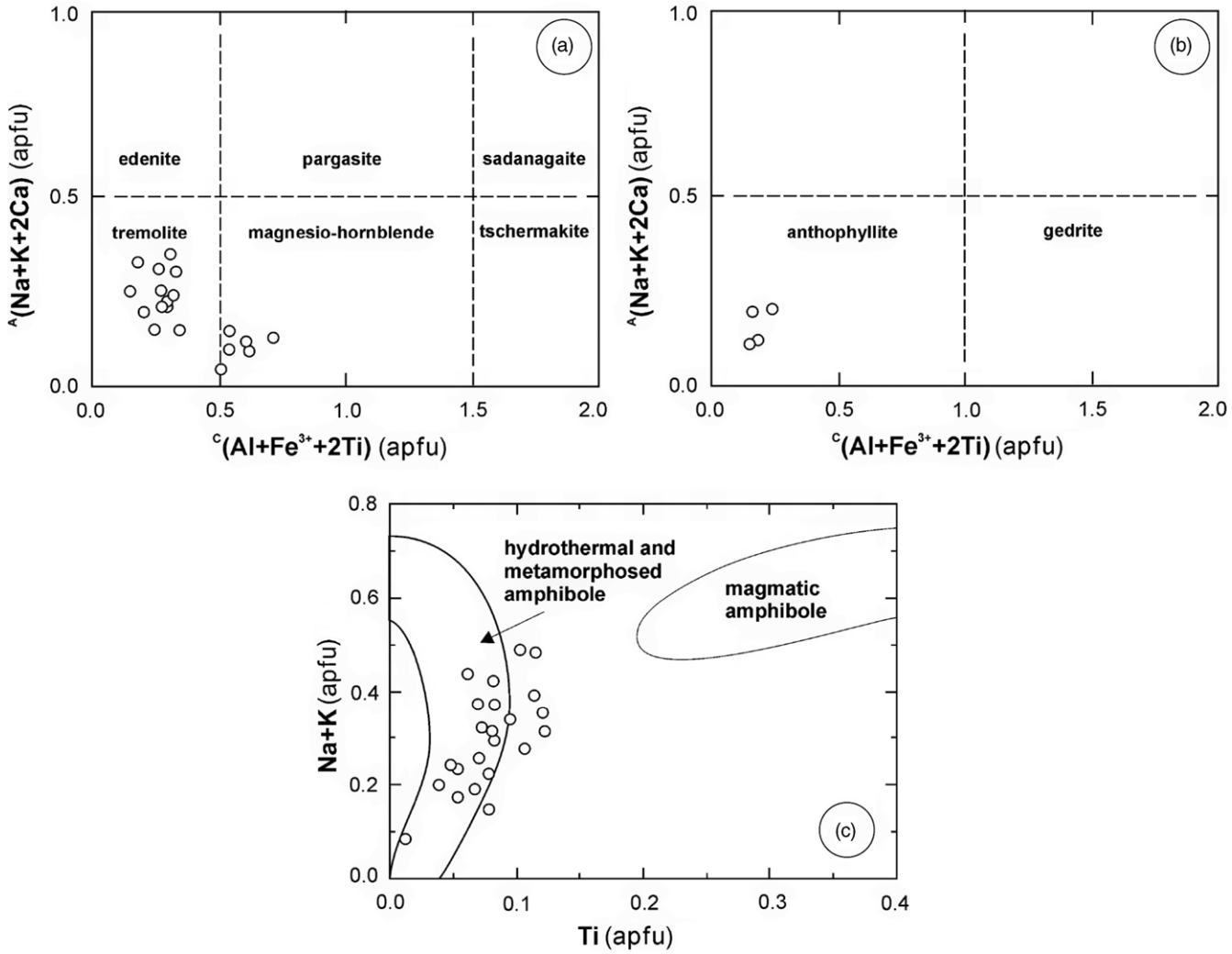

Fig. 5. Classification and discrimination diagrams for Ca monoclinic and orthorhombic Mg-Fe-Mn amphibole from the gabbroic and basaltic rocks from Mounts Kalnik and Ivanščica ophiolite mélange. (a, b) ^{A}(Na+K+2Ca – ^{C}(Al+Fe^{3+}+2Ti) plot (Hawthorne *et al.* 2012) and (c) Na+K – Ti plot (Girardeau & Mevel, 1982).

stoichiometry of prehnite is practically ideal (online Supplementary Table S1d) with FeO showing a broad compositional range (0.33–5.30 wt%). Prehnite occurs not only as an aggregate between plagioclase and amphibole, but it also fills millimetre-sized veins (Fig. 3g).

4.b.6. Pumpellyite

Pumpellyite is present in all varieties of extrusive and some intrusive rocks (online Supplementary Table S1); however, like prehnite, the amount of pumpellyite is significant only in pillow lavas that occur in hectometre-to-kilometre-sized fragments of oceanic lithosphere in the ophiolite mélange. Pumpellyite occurs as a bluish to greenish needle-like to fine-grained aggregate (Fig. 3b, e, f) commonly associated with prehnite and chlorite (Figs 4c, 6c, d, f). Fe-pumpellyite in BABB gabbro is characterized by a moderately high content of SiO_2 ($\leq$ 43.80 wt%) and variable amounts of FeO and MgO (2.78–13.91 wt% and 0.32–4.95 wt%, respectively), while the content of CaO is relatively constant (17.40–22.74 wt%) (online Supplementary Table S1d; Fig. 8a). The albitization of plagioclase delivers the necessary amount of Al for the crystallization of pumpellyite (Fig. 6d). With a somewhat lower Al/Fe ratio (online Supplementary Table S1d), pumpellyite was likely derived from the alteration of clinopyroxene (Figs 4c, 6f) or alternatively formed through the reaction of Fe(III)-rich prehnite and chlorite, giving rise to pumpellyite and quartz (Deer *et al.* 2013).

4.b.7. Zeolite

Zeolite is only present in Middle Triassic E-MORB and Middle Jurassic N-MORB ophiolite extrusive rocks (Table 2). Zeolite in basalts is fine-grained and whitish in colour, with a platy to radial habit characteristic of laumontite (Fig. 6b). Zeolite occurs as monomineralic 1.5-mm-wide veins or albitized domains of primary plagioclase. Ca-zeolite is characterized by a low content of total alkalis ($Na_2O+ K_2O < 0.42$ wt%; online Supplementary Table S1d; Fig. 8c). As per the Si/Al ratio (2.05–2.13), laumontite corresponds to the intermediate-silica type of zeolite (Campbell *et al.* 2016).

4.b.8. Other accessory phases

Titanite is an accessory phase in all ophiolitic intrusive and extrusive rocks, while in non-ophiolite rocks it is rare (Table 2). It may be found as fine-grained sub- to anhedral aggregates (up to 0.5 mm in size) associated with ilmenite and magnetite (Figs 3f, h, 4, 6). Titanite is commonly altered and transformed into dense,

https://doi.org/10.1017/S0016756822001030 Published online by Cambridge University Press

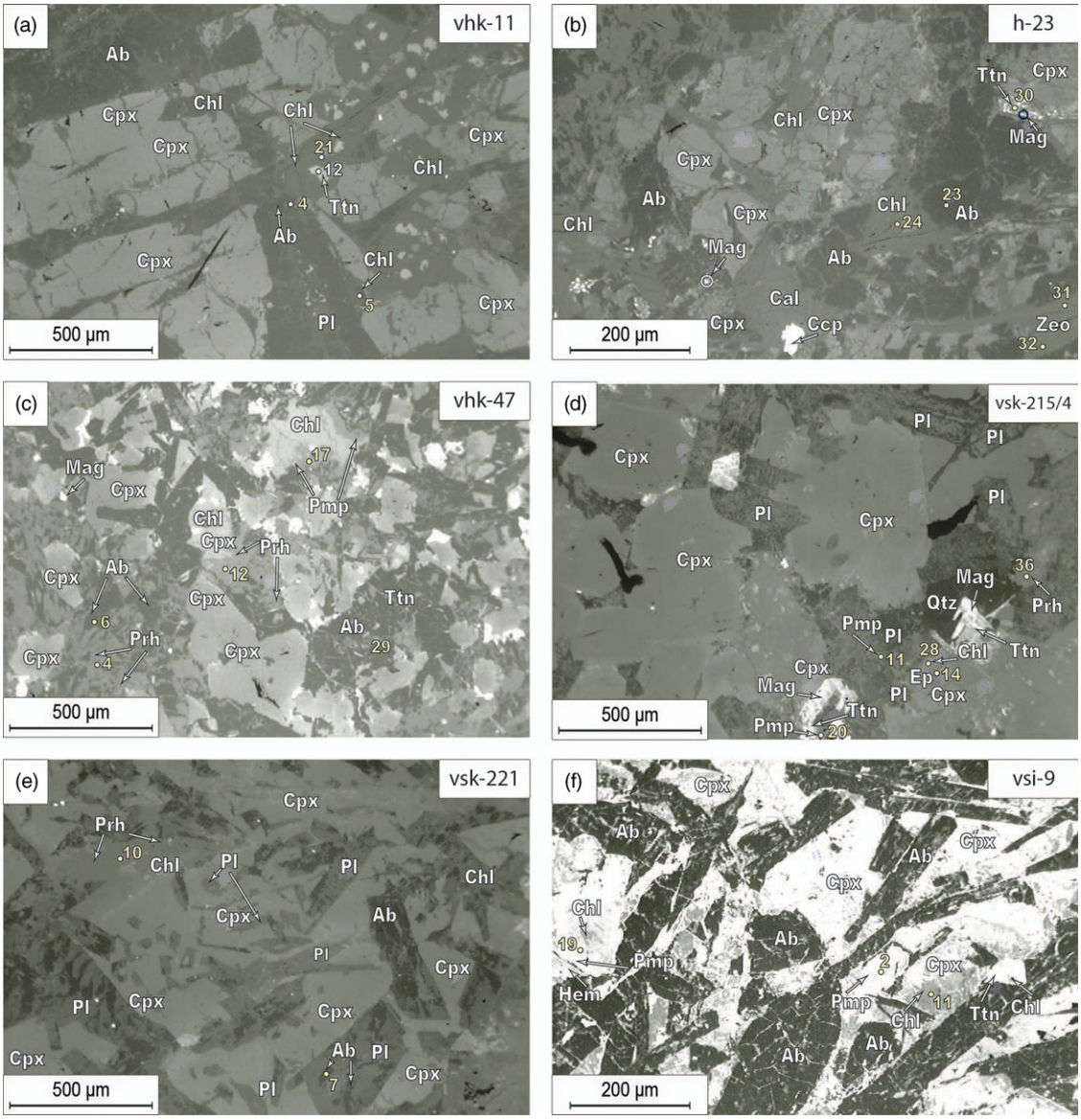

Fig. 6. (Colour online) BSE microphotographs of basalts: (a) sample vhk-11; (b) sample h-23; (c) sample vhk-47; (d) sample vsk-215/4; (e) sample vsk-221; (f) sample vsi-9 from Mounts Kalnik and Ivanščica ophiolite mélange. Numbered acquisition points correspond to the data in online Supplementary Tables S1a–1e. Legend: Ab – albite; Cal – calcite; Ccp – chalcopyrite; Chl – chlorite; Cpx – clinopyroxene (augite); Ep – epidote; Hm – haematite; Mag – magnetite; Pl – plagioclase; Pmp – pumpellyite; Prh – prehnite; Qtz – quartz; Rt – rutile; Stp – stilpnomelane; Ttn – titanite; Zeo – zeolite.

cryptocrystalline aggregates of leucoxene within plagioclase and chlorite (Fig. 3f). The composition of titanite defines it as grothite (Deer *et al.* 2013), which is a variety rich in Al, Fe and structural vacancies (Fig. 8b). The latter is reflected in low sums of total cations per formula unit (online Supplementary Table S1e). Since leucoxene commonly accompanies titanite, it is reasonable to hypothesize that leucoxene represents accumulations of cryptocrystalline titanite and Ti-oxides. Anatase has been identified by XRD in several samples of N-MORB, IAT and BABB Jurassic and Cretaceous basaltic rocks (Table 2).

Pyrite and pyrrhotite (online Supplementary Table S1e) occur in ophiolite and non-ophiolite lithologies (Table 1) as *c.* 50-µm-sized particles (Fig. 6b). Haematite and Ti-haematite, comparatively more rare than the sulphides, occur in N-MORB Upper Triassic – Middle Jurassic basalts (online Supplementary Table S1e; Fig. 6f).

4.c. Sr isotopic composition

The Sr isotopic composition of 38 Mesozoic mafic intrusives, extrusives and pyroclastic rocks is shown in Table 3. The initial isotopic ratios of Sr are calculated for the corresponding age of each sample (i.e. the assumed age of crystallization; 245–103 Ma). This age span is based on Ar/Ar and K/Ar isotopic ages of Lugović *et al.* (2015), Slovenec *et al.* (2011) and Slovenec & Šegvić (2021). The $^{87}Sr/^{86}Sr$ ratios show large variations (0.703208–0.718603) based on (a) the location of samples, (b) the type of geotectonic environment, and (c) the age of crystallization of the rocks and the degree of alteration.

The most prominent variations in Sr initial isotopic ratios ($(^{87}Sr/^{86}Sr)_t = 0.703195–0.710252$; Fig. 9) are of Middle Triassic non-ophiolite basalts/andesites and tuffs, and pyroclastic rocks (CAB). A somewhat narrower variation range of Sr initial isotopic ratios (0.703725–0.708406) occurs in Middle–Upper Jurassic and

https://doi.org/10.1017/S0016756822001030 Published online by Cambridge University Press

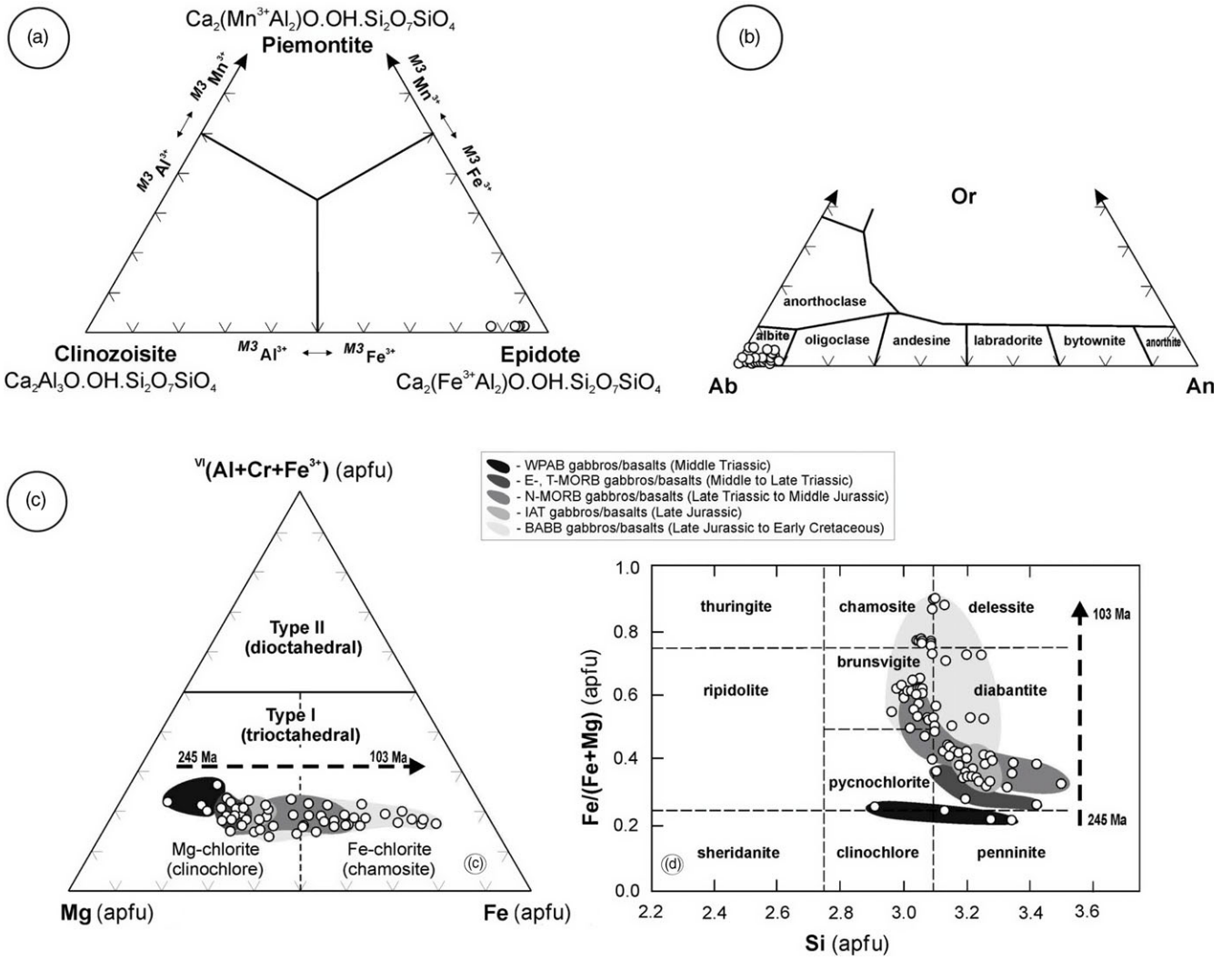

Fig. 7. Classification diagram for (a) epidote group minerals (Armbruster *et al.* 2006); (b) feldspar (Ab–An–Or plot; Deer *et al.* 2013) from gabbroic and basaltic rocks from Mounts Kalnik and Ivanščica ophiolite mélange; and chlorite classification diagrams (c) Mg–Fe–^{VI}(Al+Cr+Fe^{3+}) (Zane & Weiss, 1998) and (d) Fe/(Fe+Mg)–Si (after Sun *et al.* 2019).

Lower Cretaceous intrusive and extrusive orogenetic rocks (IAT, BABB; Fig. 9). On the other hand, Middle Triassic – Middle Jurassic mafic ophiolite intrusive and extrusive rocks that crystallized in anorogenic domains (WPAB, E-MORB, T-MORB, N-MORB) are characterized by a more narrow range of Sr initial isotopic ratios (($^{87}Sr/^{86}Sr)_t = 0.703122–0.705632$; Fig. 9). In these rocks, the ($^{87}Sr/^{86}Sr)_t$ values are generally the lowest, reflecting their weakest alteration intensities.

4.d. REE geochemistry of chlorite and pumpellyite

Chlorite and, to a certain degree, pumpellyite occur in most of the analysed samples (Table 2). These phases were used to investigate the mobility of REE during alteration processes that postdate the formation of igneous host rocks. Three samples of non-ophiolite basalts were deemed representative because of the various textures involving chlorite and pumpellyite. Textural differences are likely the result of a multitude of nascent hydrothermal events, which show contrasting REE signatures. The REE geochemistry of chlorite and pumpellyite are given in online Supplementary Table S2.

REE concentrations of chlorite (online Supplementary Fig. S1a–c) display consistent values where the standard deviation is on average less than 15% for each element (online Supplementary Table S2). The REE content of chlorite is low (45–50 ppm), ranging over *c.* 0.45–3.17 relative to chondrite (Boynton, 1984; Fig. 10). The Eu anomaly is moderate ($Eu_{chon}/Eu_{chon}^* = 0.73–1.11$; $Eu_{chon}^* = (Sm_{chon}+Gd_{chon}) \times 0.5$) and the REE normalization curves are somewhat similar to N-MORB with a substantial depletion in LREE ($La_{chon}/Yb_{chon} = 0.26–0.33$).

Chondrite-normalized REE curves of euhedral chamosite phenocrysts show a REE enrichment (1–100 × chondrite), pronounced negative Eu anomalies ($Eu_n/Eu_n^* = 0.35–0.46$) and negative Ce anomalies ($Ce_{chon}/Ce_{chon}^* = 0.001–0.010$; $Ce_{chon}^* = (La_{chon}+Pr_{chon}) \times 0.5$) (Fig. 10). Chlorite is of hydrothermal origin in the non-ophiolite basalts (Table 2), as euhedral pumpellyite (online Supplementary Fig. S1d) in the hypocrystalline matrix consisting of chlorite and albite is also present. Chondrite-normalized REE patterns of pumpellyite are similar to those of boninite from ophiolite complexes (Saccani & Tassinari, 2015; Slovenec & Šegvić, 2018) outlining concave-upwards (U-shape) profiles with a slight light REE (LREE; $La_{chon}/Sm_{chon} = 3.14–3.71$) and heavy REE (HREE; $Tb_{chon}/Lu_{chon} = 0.38–0.89$) enrichment at levels of 9.01–36.06 times relative to chondrite. Abundances of medium REE (MREE) in this case are depleted with regards to HREE

https://doi.org/10.1017/S0016756822001030 Published online by Cambridge University Press

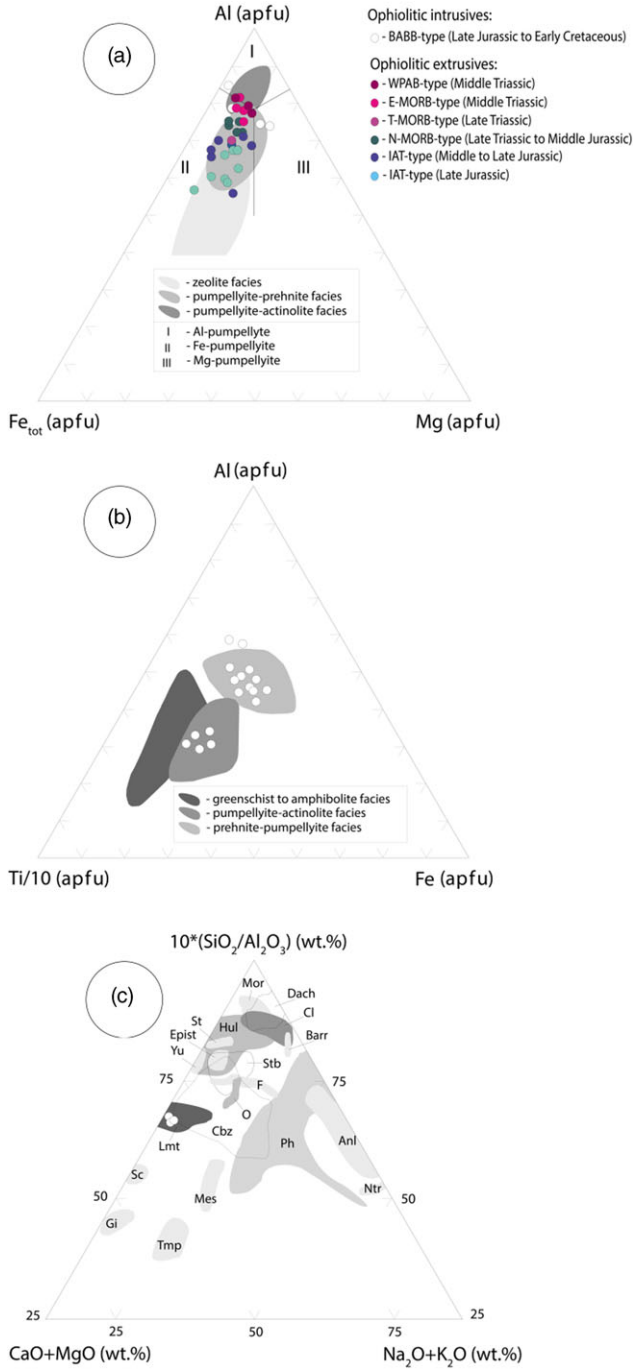

Fig. 8. (Colour online) Classification diagram for (a) pumpellyite, (b) titanite and (c) zeolite from gabbroic and basaltic rocks from Mounts Kalnik and Ivanščica ophiolite mélange. Pumpellyite Fe_{tot}–Mg–Al plot after Coombs *et al.* 1976). Compositional fields of pumpellyite from the East Taiwan Ophiolite (zeolite facies), the Olympic Peninsula (prehnite–pumpellyite facies) and the Taveyannaz Formation (upper prehnite–pumpellyite and pumpellyite– actinolite facies) are taken from Coombs *et al.* (1976) and Rahn *et al.* (1994), respectively. The discrimination diagram (Ti/10)–Fe–Al for titanite with compositional fields of metamorphic facies/environments is taken from Calderón *et al.* (2013). Zeolite CaO+MgO – Na_2O+K_2O – $10\times(SiO_2/Al_2O_3)$ plot with compositional fields after Bastias *et al.* (2016). Anl – analcime; Barr – barrerite; Cbz – chabazite; Cl – clinoptilolite; Dach – dachiardite; Epist – epistilbite; F – faujasite; Gi – gismondine; Hul – heulandite; Lmt – laumontite; Mes – mesolite; Mor – mordenite; Ntr – natrolite; O – offretite; Ph – phillipsite; Sc – scolecite; St – stellerite; Stb – stilbite; Tmp – thomsonite; Yu – yugawaralite.

(Fig. 10). A prominent positive Eu anomaly (Eu_{chon}/Eu_{chon}^* = 1.17–1.74) is also present.

5. Discussion

5.a. Mineralogical changes and their implications

Taking into account all ophiolites and non-ophiolitic volcanic lithologies, the intensity of hydrothermal alteration seems to be strongest in the ophiolite extrusive rocks (Table 2). The alteration intensity of the rocks, which can be equated to an increase in the seawater–rock interaction rate, may be monitored through the oscillation of the initial Sr isotopic ratios. This feature serves as an alteration index (Bickle & Teagle, 1992) of studied Mesozoic lithologies (Fig. 9). This is recognizable in Mesozoic mafic intrusive and extrusive rocks; namely, the oldest ophiolite rocks are part of anorogenic domains (WPAB, E-MORB, T-MORB, N-MORB) that are related to the extension of the oceanic lithosphere and the formation of the western branch of the Neotethys (Slovenec *et al.* 2011; Fig. 11a,b). These rocks are weakly to moderately altered with a dwindling Middle Triassic – Middle Jurassic Sr alteration trend (Fig. 9). This seafloor spreading system was succeeded by Neotethyan intraoceanic subduction during the Middle Jurassic Epoch (Bathonian; Fig. 11c). Related suprasubduction processes during the Late Jurassic Epoch resulted in the development of orogenic domains (IAT, BABB; Slovenec *et al.* 2011). A distinctly increasing Sr alteration trend is documented in these rocks, delineating a growing impact of seawater that lasted through latest Jurassic and Early Cretaceous time (Fig. 11d). Described trends are well correlatable with changes in seawater composition during the Mesozoic Era (Fig. 9; Kovács *et al.* 2020). In contrast to ophiolite rocks, Middle Triassic non-ophiolite basalts and tuffs (CAB; Fig. 11a) from the active continental margin indicate a broad range of alteration intensities devoid of any obvious trend (Fig. 9). Another useful parameter that may provide insights into the alteration dynamics is the Sr/Ca ratio (Scambelluri *et al.* 2001). Its relatively high values (25–74) in Middle Triassic – Middle Jurassic ophiolite mafic intrusives and extrusives rocks that crystallized in anorogenic domains (WPAB, E-MORB, T-MORB, N-MORB), compared with somewhat lower Sr/Ca values (16–49) in Upper Jurassic to Lower Cretaceous suprasubduction series rocks, suggest a gradual decrease in the degree of albitization and plagioclase alteration, which is in line with the earlier findings of Slovenec *et al.* (2011). This trend may further outline a progressive dwindling in depths at which hydrothermal processes occurred, thus suggesting an ocean-floor transition from the greenschist to zeolite facies metamorphism during Middle Triassic – Early Cretaceous time.

Hydrothermal sulphide-oxide systems are essentially controlled by mineral-fluid equilibria, which may provide valuable information on the prevailing chemical and physical characteristics of the mineralizing fluid such as elemental composition, temperature, pH, fO_2, dilution and cooling rates (e.g. Rottier *et al.* 2016). Middle Triassic – Lower Cretaceous ophiolite rocks show variable amounts of sulphides and oxides (Table 2; online Supplementary Table S1e). Weakly to moderately altered non-orogenic Ladinian–Bajocian ophiolite rocks (WPAB, E-MORB, T-MORB and N-MORB; Fig. 11a,b) contain either sulphides (pyrite or pyrrhotite) or oxides (haematite or magnetite). Conversely, orogenic

https://doi.org/10.1017/S0016756822001030 Published online by Cambridge University Press

Table 3. Sr isotopic data of Mesozoic ophiolitic and non-ophiolitic basalts/andesites and tuffs from the mountains of NW Croatia.

Sample	Locality	Rock	Geotectonic affinity	$^{87}Rb/^{86}Sr^{a}$	$^{87}Sr/^{86}Sr$ (2σ)	Rb	Sr	$^{87}Sr/^{86}Sr_{(t)}$	Age (Ma)^{b,c}
vsk-242	KA	GB	N-MORB	0.032506	0.703208 (10)	1	89	0.703122	185
mc-2	ME	GB	IAT	0.348215	0.708470 (26)	16	133	0.708026	161
vsk-228/2	KA	GB	IAT	0.186341	0.708306 (10)	15	233	0.707919	146
vsk-229/1	KA	GB	BABB	0.059583	0.706844 (08)	7	340	0.706753	108
vsk-229/11	KA	GB	BABB	0.120587	0.706968 (09)	11	264	0.706783	108
gi-2	IV	GB	BABB	0.020527	0.707666 (14)	1	141	0.707634	108
vsi-8/3	IV	GB	BABB	0.03487	0.707412 (16)	2	166	0.707361	103
ce-11	IV	TU	CAB	0.403301	0.707562 (10)	51	366	0.706217	245
ce-16	IV	TU	CAB	1.130143	0.707523 (11)	123	315	0.707069	245
tskg-1/2b	KG	AB	CAB	2.529483	0.718603 (11)	55	63	0.709896	242
tskg-10	KG	AB	CAB	1.994647	0.717118 (10)	42	61	0.710252	242
tsi-2	IV	BA	CAB	0.209691	0.705633 (21)	15	207	0.704911	242
d-11	IV	AB	CAB	0.106458	0.705649 (15)	11	299	0.705283	242
v-6	IV	BA	CAB	0.161359	0.705518 (11)	15	269	0.704963	242
čo-11	IV	TU	CAB	1.977103	0.716054 (16)	43	63	0.709248	242
tss-2	ST	AB	CAB	2.857552	0.714845 (09)	60	61	0.705008	242
kl-40b	ŽU	TU	CAB	2.585409	0.712426 (15)	75	84	0.703526	242
bz-32	ŽU	TU	CAB	2.56929	0.712039 (11)	63	71	0.703195	242
92-16	SG	BA	WPAB	0.051982	0.705445 (09)	3	167	0.705271	242
sb-9	ME	BA	WPAB	0.124912	0.705851 (14)	6	139	0.705421	242
kb-6	KA	BA	WPAB	0.075051	0.705220 (12)	9	347	0.705133	236
vsk-207b	KA	BA	E-MORB	0.012861	0.705676 (08)	5	225	0.705632	239
h-33/1	KA	BA	E-MORB	0.091655	0.705489 (10)	7	221	0.705177	239
ke-2/1	KA	BA	T-MORB	0.083699	0.705207 (13)	7	242	0.704933	230
ja-2/2	KA	BA	N-MORB	0.251623	0.705423 (08)	8	92	0.704636	220
vsi-6/5	IV	BA	N-MORB	0.220446	0.704277 (10)	8	105	0.704634	175
t-51/1	ME	BA	N-MORB	0.10918	0.704001 (25)	6	159	0.703729	175
vs-113/3	ME	BA	N-MORB	0.377399	0.704423 (09)	12	92	0.703511	170
vh-1001/1	ME	BA	N-MORB	0.284464	0.704057 (10)	10	101	0.703365	170
vs-486	ME	BA	IAT/BABB	0.344491	0.705584 (13)	15	126	0.704776	165
vs-328	ME	BA	IAT/BABB	0.101486	0.703963 (10)	2	57	0.703725	165

(*Continued*)

Table 3. (*Continued*)

Sample	Locality	Rock	Geotectonic affinity	$^{87}Rb/^{86}Sr^{a}$	$^{87}Sr/^{86}Sr$ (2σ)	Rb	Sr	$^{87}Sr/^{86}Sr_{(t)}$	Age (Ma)[b,c]
t-23b/1	SG	BA	IAT/BABB	0.131445	0.707465 (12)	14	306	0.707157	165
jf-34/1	SG	BA	IAT/BABB	0.273076	0.708722 (14)	10	106	0.708081	165
h-26	KA	BA	IAT	0.02679	0.704254 (05)	1	108	0.704191	165
m-17	ME	BA	IAT	0.368777	0.704734 (22)	13	102	0.703875	162
got-6/1	IV	BA	IAT	0.030793	0.708474 (12)	1	94	0.708406	155
m-18/1	ME	BN	IAT	0.141182	0.707422 (15)	2	41	0.707111	155
vh-49/3	ME	BN	IAT	0.096465	0.706427 (11)	1	30	0.706214	155

[a] $^{87}Rb/^{86}Sr$ ratios calculated from Rb and Sr ICP-MS concentrations (displayed in ppm) following: $^{87}Rb/^{86}Sr = (Rb/Sr) \times [2.6939 + 0.2832 \times (^{87}Sr/^{86}Sr)]$.

[b] Initial $^{87}Sr/^{86}Sr_{(t)}$ calculated assuming $\lambda_{Rb} = 1.42 \times 10^{-11}$ a^{-1}.

[c] Part of the data from Slovenec *et al.* (2011, 2012).

AB – andesite-basalt; BA – basalt; BABB – back-arc basin basalts; BN – boninite; CAB – calc-alkaline basalts; DI – diabase; E-MORB – enriched mid-ocean-ridge basalts; GB – gabbro; IAT – island-arc tholeiites; KA – Kalnik Mount; KG – Kuna Gora Mount; IV – Ivanščica Mount; ME – Medvednica Mount; N-MORB – normal mid-ocean-ridge basalts; SG – Samoborska Gora Mount; ST – Strahinjščica; T-MORB – transitional mid-ocean-ridge basalts; TU – tuff; WPAB – within-plate alkaline basalts; ŽU – Žumberak Mount.

Bathonian–Valangian highly altered ophiolite rocks (IAT and BABB; Fig. 11c,d) are practically devoid of sulphides, while oxide minerals are commonly present. Sulphide precipitation must have been triggered by a temperature decrease of the mineralizing fluid, coupled with decreased sulphide solubility below 300 °C (Henley *et al.* 1984). Cooling is normally caused by a drop in pressure associated with fluid ascending in the hydrothermal system or cold seawater mixing (Capuano & Cole, 1982). This in turn makes the pH of hydrothermal fluid decrease following sulphide precipitation (Akaku *et al.* 1991). The moderately to highly reducing character of sulphide-producing fluids and reduced pH causes redox-sensitive phases such as Fe oxides to dissolve (Henley *et al.* 1984). This likely explains the lack of haematite and magnetite in sulphide-bearing samples (Table 2). Sulphide-producing hydrothermal fluids stem from deep-seated portions of an active ocean ridge while parageneses free of sulphides are related to the relatively oxidizing environment prevailing at shallow levels of the hydrothermal system (Fouquet *et al.* 2018). Because the latter pertains to Bathonian–Valangian orogenic ophiolite rocks, it is hypothesized that an intensive suprasubduction tectonism facilitated access to the hot recharge zone of the hydrothermal system without changing the redox character of the mineralizing fluid. This is consistent with Sr/Ca values in Upper Jurassic – Lower Cretaceous rocks, which called for a progressive shrinkage of depths associated with seafloor metamorphism.

5.a.1. Basaltic ophiolitic and non-ophiolitic rocks

The intrinsic textural and structural characteristics of basaltic rocks were largely preserved during hydrothermal metamorphism, despite significant mineralogical changes. Submarine effusive eruptions resulted in an instantaneous quenching of lava to form pillow lavas (e.g. Fujibayashi *et al.* 2014). As the new seafloor was produced at mid-ocean ridges during Ladinian–Bajocian time (Fig. 11b), the high permeability of the newly formed oceanic crust allowed ample quantities of water to penetrate and acquire heat from the crust (Kuhn *et al.* 2017). At high temperatures, hydrothermal upwelling fluids eventually reacted with the oceanic crust to form new phases or recrystallized existing phases, which accommodated ascending pathways of venting fluids. Hydrothermal mineral zones contain typical parageneses of very-low- (200–360 °C) to low-grade (360–500 °C) metamorphic facies (Slovenec *et al.* 2012).

In the hydrothermal seafloor setting, albitization of plagioclase (online Supplementary Table S1c) commonly takes place in zones of high seawater activity at moderate temperatures and/or upwelling zones where Si-Na-rich and Ca-poor fluids, which stem from high-temperature zones at depth, are cooled down during their ascent (Von Damm *et al.* 1985; Ray *et al.* 2009). The albitization-related release of Ca facilitated crystallization of hydrothermal Ca-bearing phases such as calcite, epidote, Al-pumpellyite, Ca-zeolite, zoisite/clinozoisite and titanite. The high amounts of chlorite in primary plagioclase (Fig. 4f) indicate that the albitization of plagioclase and chloritization were penecontemporaneous and mutually dependent processes. Based on chlorite geothermometry (Inoue *et al.* 2018), temperatures ranged over 92–489 °C (interstitial chlorite, online Supplementary Fig. S2; Fig. 7d). The phase chemistry of the hydrothermal chlorite reflects the geotectonic affinity of host rocks that can be traced during a span of *c.* 150 Ma from the formation of the initial oceanic lithosphere during Middle Triassic time, through the spreading of Neotethys which lasted until Middle Jurassic time and, lastly, until Late Jurassic – Early Cretaceous intraoceanic subduction

https://doi.org/10.1017/S0016756822001030 Published online by Cambridge University Press

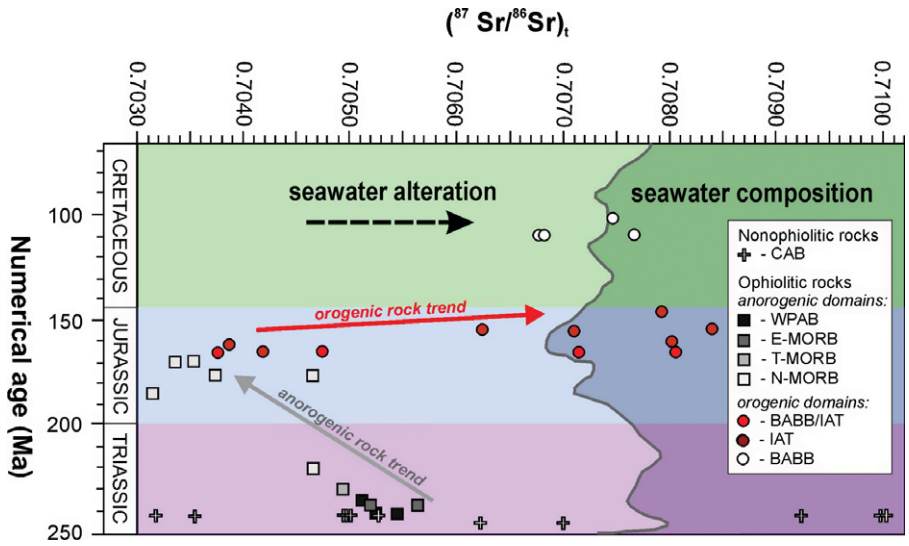

Fig. 9. (Colour online) Initial $^{87}Sr/^{86}Sr$ isotope ratios diagram for Mesozoic ophiolitic and non-ophiolitic basalts/andesites and tuffs from the NW Croatia mountains. The record of Mesozoic seawater $^{87}Sr/^{86}Sr$ taken from Peucker-Ehrenbrink & Fiske (2019). Part of the data originate from), and Slovenec *et al.* (2011, 2012).

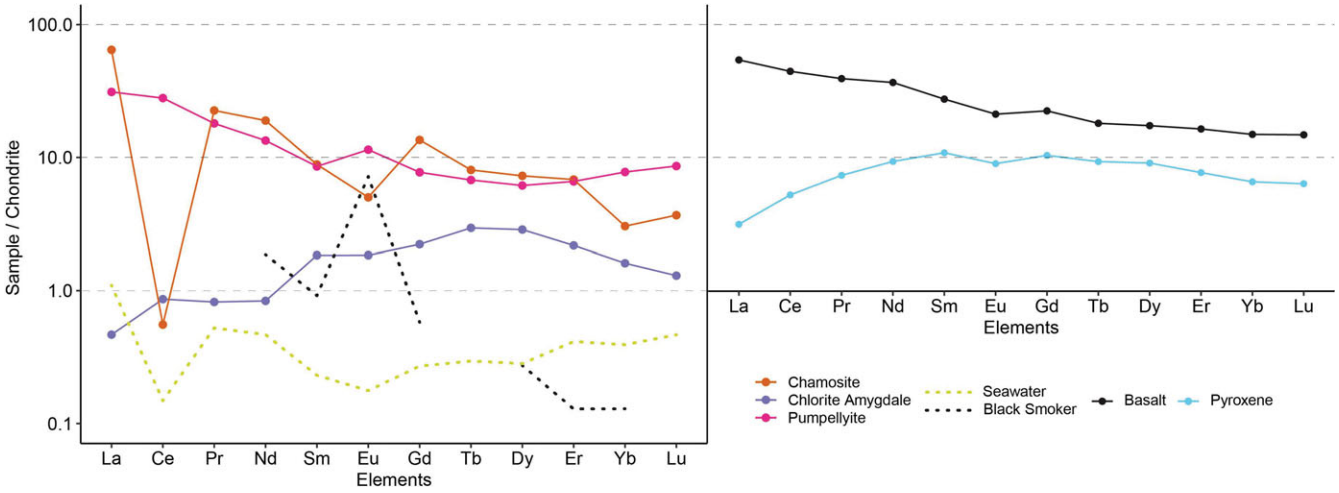

Fig. 10. (Colour online) The chondrite-normalized plots (Boynton, 1984) for hydrothermal chlorite and pumpellyite as well as the relict clinopyroxene and whole-rock basalt rocks from the study area. Dashed lines represent normalization plots of black-smoker solutions (East Pacific Rise, Michard *et al.* 1983) and seawater (Høgdahl *et al.* 1968).

(Fig. 11a–d). Accordingly, a clear downwards trend in the Mg content (clinochlore) and an increase in Fe^{2+} (chamosite) is obtained starting with WPAB (Middle Triassic, Illirian) through E-MORB (Middle Triassic, upper Fassanian – lower Longobardian), T-MORB (Upper Triassic, middle–upper Carnian), N-MORB (Upper Triassic, upper Carnian – middle Norian to Middle Jurassic, Bajocian), IAT (Middle Jurassic, upper Bajocian – Oxfordian; Upper Jurassic, Callovian–Tithonian) and BABB (Lower Cretaceous, Albian; Fig. 7c, d) gabbro and/or basalt. This correlates well with the petrographic observations indicating a more intensive alteration of clinopyroxene and albitization of plagioclase coupled with increased abundances of chlorite in Upper Jurassic and Lower Cretaceous extrusive and intrusive rocks compared with those of Middle Triassic and Middle Jurassic age (Table 2). Reconciling the chlorite phase chemistry and its crystallization temperatures, an inference can be made about high-temperature post-magmatic hydrothermal conditions (prehnite-actinolite facies; Mg no.$_{chl}$ > 57; online Supplementary Table S1b) that existed during Middle–Late Jurassic time during an intensive intraoceanic subduction in the western segment of the Neotethys (Fig. 11c, d). This resulted in a great diversity of hydrothermal parageneses in the rocks of the ophiolite mélange of the Sava Unit (Slovenec *et al.* 2011) with abundant crystallization of prehnite (online Supplementary Table S1d) in the range 190–340 °C (Liou *et al.* 1985), which implies an origin at an early stage in the alteration history of the Sava Unit oceanic lithosphere. A somewhat lower hydrothermal temperature then prevailed (180–250 °C, i.e. prehnite-pumpellyite facies; Mg no.$_{chl}$ < 57; online Supplementary Table S1b) during Late Jurassic – Early Cretaceous time in a newly established back-arc extensional regime (Fig. 11d). Under these conditions in effusive ophiolite rocks (dominantly in pillow lavas) along with chlorite, the dominant alteration phase is pumpellyite (online Supplementary Table S1d). As per the criteria of Liou *et al.* (1985) the studied Al-poor pumpellyite (Al ≤ 2.290 apfu) formed at temperatures ranging over 160–320 °C, thus corroborating prehnite-pumpellyite facies conditions (Fig. 8a). The pressure needed for the crystallization of prehnite-pumpellyite-bearing assemblages is 0.1–0.2 GPa (Schiffman & Liou, 1983). Conversely, less common Al-pumpellyite (Al > 2.290 apfu) with a high ratio of Al/Fe_{tot} (4.14–6.90) present in zeolite-free parageneses likely formed at a temperature not significantly lower than 250 °C and at pressures of 0.3–0.5 GPa.

https://doi.org/10.1017/S0016756822001030 Published online by Cambridge University Press

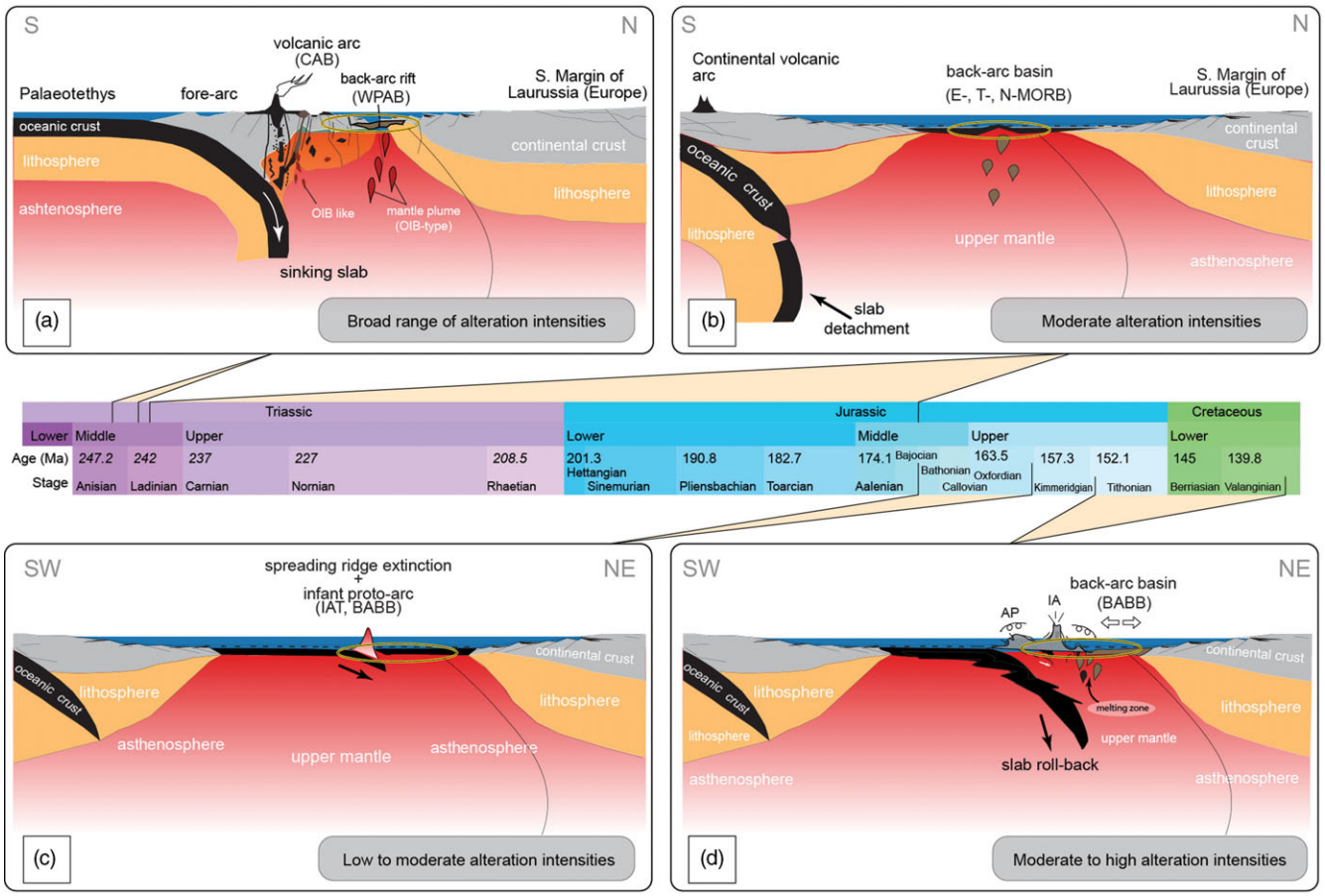

Fig. 11. (Colour online) Schematic geodynamic model for interaction of (a) active continental margin magmatic activity (ensialic volcanic arc magmatism) and roughly contemporaneous proto back-arc rifting, (b) active spreading, (c) subduction of an active ocean ridge and (d) evolved subduction stage with initiation of an island arc and formation of the subsequent ensialic marginal (back-arc) basin in Meliata-Maliak-Dinaric-Vardar ocean system (modified from Slovenec *et al.* 2011, Lugović *et al.* 2015; Slovenec & Šegvić, 2021). Scale is approximate. IA – island arc (infant proto-arc/island-arc system); BAB – back-arc basin; AP – accretionary prism; WPAB – within-plate alkaline basalts; BABB – back-arc basin basalts; CAB – calc-alkaline basalts; E-MORB – enriched mid-ocean-ridge basalts; IAT – island-arc tholeiites; N-MORB – normal mid-ocean-ridge basalts; OIB – ocean-island basalts; T -MORB – transitional mid-ocean ridge basalts.

This supports the idea of prehnite-actinolite facies conditions at comparatively higher alteration depths (Liou *et al.* 1985). The variations in the Al content of pumpellyite are largely the result of the Al-Fe(III) substitution that indicates that, in addition to pressure and temperature, fO_2 exercises a further control on pumpellyite stability (Inoue & Utada, 1991). Indeed, the formation of Al-pumpellyite occurs at lower fO_2 (Schiffman & Liou, 1983), which is consistent with a proposed crystallization at high depths. It is therefore reasonable to infer that during the Mesozoic Era (Middle Triassic WPAB and E-MORB through Upper Jurassic suprasubduction extrusive rocks) pumpellyite became progressively impoverished in Al (Fig. 8a; online Supplementary Table S1d). This indicates a gradual decrease in crystallization temperatures at lower depths of hydrothermal activity.

In a near-surface environment in contact with hydrothermal fluids, during Triassic–Jurassic ocean crust spreading as well as Upper Jurassic subduction, titanitization must have taken place under conditions of prehnite-pumpellyite facies metamorphism (Fig. 8b). This is corroborated by the titanite chemistry (online Supplementary Table S1e) from effusive rocks that contain relatively high abundances of Al (0.12–0.18 apfu) and Fe (0.05–0.08 apfu) as well as low sums of total cations. Al and Fe commonly substitute for Ti, which takes place at temperatures ranging over 180–320 °C as suggested by Enami *et al.* (1993) who revealed that, in metamorphic systems, the average Al + Fe^{3+} content of titanite increases systematically with decreasing temperatures.

In a continuous sequence of ocean-floor metamorphism characterized by conditions of low-pressure (< 1 GPa) and temperature (≤ 240 °C) (Liou *et al.* 1985) paragenesis, ophiolite effusive rocks of the investigated area are sporadically zeolitized to produce laumontite (Table 2; Fig. 8c). This process was detected during the Middle Triassic – Middle Jurassic oceanization (Fig. 11b). The origin of this Ca-zeolite is related to the fluid-induced re-equilibration and the breakdown of Ca-rich plagioclase to secondary phases (Deer *et al.* 2013). Considering that the lowest temperature zones of thermal metamorphic aureoles in volcanic terranes typically contain laumontite, it may be hypothesized that its formation temperature was *c.* 125 °C. This correlates well with a crystallization temperature of diagenetic laumontite from deep-buried clastic reservoirs that grew on the volcanoclastic substrate (e.g. Ilijima & Utada, 1972).

5.a.2. Gabbroic ophiolitic rocks

In gabbroic ophiolite rocks, however, which are thoroughly affected by the seafloor hydrothermal activity, a multi-phase

https://doi.org/10.1017/S0016756822001030 Published online by Cambridge University Press

alteration sequence has been identified with distinct alteration assemblages. The first phase records deuteric changes at high subsolidus temperatures where clinopyroxene (augite) is replaced by hornblende (Fig. 3b). The formation of deuteric magnesiohornblende (Figs 4a, b, d, f, 5a) represents the late magmatic crystallizate formed at temperatures not exceeding 500 °C. This event marked the onset of the ocean-floor metamorphism (Coleman, 1977), and is related to the period of Triassic–Jurassic oceanization, Upper Jurassic subduction and Lower Cretaceous back-arc extension (Fig. 11b–d). In some samples of gabbro, a second reaction rim consisting of anthophyllite occurs around hornblende (online Supplementary Table S1a; Figs 4d, 5b). It follows that the altered gabbro made of deuteric hornblende + tremolite/actinolite + anthophyllite + albite + chlorite ± titanite formed under pumpellyite-actinolite to middle greenschist facies conditions (200–450 °C, 0.2–0.4 GPa; Liou *et al.* 1985). These conditions stem from intensive tectonic activity and crust emplacement in the Neotethyan arc and back-arc settings, which formed during Late Jurassic and Early Cretaceous time (Slovenec *et al.* 2011; Lugović *et al.* 2015; Fig. 11d). The next alteration stage is typical of the greenschist facies and includes the development of albite, tremolite, epidote, chlorite and serpentine that grew on a primary substrate of plagioclase, clinopyroxene and/or tschermakite-magnesiohornblende and olivine (Figs 3b, 4a–f; online Supplementary Tables S1a–S1c). Interstitial chlorite formation temperatures largely of *c.* 250 °C (online Supplementary Fig. S2) are in line with such inferences. This stage is related to Upper Jurassic subduction and Lower Cretaceous back-arc extension (Fig. 11c, d). Epidote-bearing parageneses containing albite, chlorite, prehnite ± tremolite (Fig. 3d, e) and their microtexture, as well as substitution values of Fe^{3+} in the octahedral site (i.e. pistacite component) of epidote ($Fe^{3+}/(Fe^{3+}+Al) = 0.29–0.31$) are all indicative of a relatively high crystallization temperature (320–420 °C) irrespective of the host rock and low rock to seawater ratios (Liou *et al.* 1985). This correlates well with the experimental results of Berndt *et al.* (1989), and conforms with low-pressure conditions ranging over 0.1–0.2 GPa. Accordingly, the process of epidotization belongs to the transitional zone between the prehnite-actinolite and lower greenschist facies. Epidote and associated chlorite are therefore suggested to be products of reactive components derived from plagioclase and clinopyroxene on the one hand, and high-temperature hydrothermal fluids on the other (Deer *et al.* 2013). This phase (clinopyroxene) further includes the re-equilibration of Ti-rich spinel through the exsolution of minute pseudobrookite lamellae. The final alteration step produced prehnite, pumpellyite, titanite and illite/mica (Fig. 4c, f) during Upper Jurassic – Lower Cretaceous back-arc extension (Fig. 11d). Pumpellyite is either Fe- or Al-rich, meaning it was formed after clinopyroxene or plagioclase, respectively (Ishizuka, 1991). The formation of pumpellyite, irrespective of its chemistry, denotes the transition between the zeolite and greenschist facies (e.g. Kamimura *et al.* 2012).

5.a.3. Controls on the ocean-floor hydrothermal mineralogy

While the fluid temperature, pressure, composition and oxygen fugacity exercise an important role in the evolution of hydrothermal assemblages, it is the chemistry of magmatic host lithologies that sets the trajectories of mineralogical alterations documented here. The difference in chemistry between the two major mafic rock suites (i.e. ophiolite and non-ophiolite basalts/andesites and tuffs of the active continental margin; Table 2) is evident. The SiO_2 content for ophiolites ranges over *c.* 46–50 wt%, TiO_2 is *c.* 2 wt%, while CaO and K_2O contain up to 11 and 1.5 wt%, respectively (e.g. Slovenec *et al.* 2011; Slovenec & Šegvić, 2018). Conversely, the composition of non-ophiolitic basalts/andesites and tuffs (e.g. Goričan *et al.* 2005; Slovenec & Šegvić, 2021) is marked by higher levels of SiO_2 (*c.* 53–57 wt%) and K_2O (*c.* 3–6 wt%), whereas CaO and TiO_2 do not exceed *c.* 5.5 and 1 wt%, respectively. Compositional differences are reflected in the mineralogy of the hydrothermal parageneses of non-ophiolite basalts/andesites and tuffs, which are dominated by quartz and K-bearing phyllosilicates, while ophiolite rocks are virtually free of quartz and mica, and are more enriched in TiO_2-phases and Ca-silicates such as prehnite, pumpellyite and laumontite (Table 2). This is consistent with a closed architecture of the hydrothermal systems of the Dinaridic Neotethys where fluid fluxes were likely confined within a single lithological unit, yielding relatively uniform but contrasting hydrothermal assemblages in ophiolite on the one hand, and non-ophiolite basalts/andesites and tuffs on the other. A plausible explanation may be the lack of deep normal faulting that channelizes fluid flows to deeper crustal levels (e.g. Schiffman & Staudigel, 1994), possibly as a result of rapid transitions in the Dinaridic Neotethys geotectonic setting, changing from active ridge magmatism to an intraoceanic subduction environment and island-arc volcanism (Slovenec *et al.* 2011; Šegvić *et al.* 2014). Finally, petrographic and EMPA/SEM observations yielded no evidence of alteration of hydrothermal phases formed in ophiolite and non-ophiolite basalts/andesites and tuffs, which is consistent with the closed hydrothermal system hypothesis advocated above (e.g. Morad *et al.* 2010). Furthermore, our XRD investigation shows that illite-smectite (or smectite) commonly occurs in non-ophiolitic rocks, whereas Mg-phyllosilicates (chlorite-smectite, vermiculite, lizardite, palygorskite/sepiolite) dominate ophiolite rocks (Table 2). Because of their submicron size, both illite-smectite and Mg-phyllosilicates formed diagenetically through the weathering of mica and chlorite/amphibole, respectively. This took place following the emplacement of these rocks, which is consistent with a recent investigation of the ophiolite mélange of the study area that, based on the Kübler and Árkai indices, indicates sheet silicates of the mélange are solely diagenetic in origin (Judik *et al.* 2005).

5.b. Chlorite and pumpellyite REE geochemistry

The normalized REE content of seawater (Høgdahl *et al.* 1968) and that of modern hydrothermal fluids (black smoker) (Michard *et al.* 1983; Michard & Albarède, 1986) with reference to REE abundances in analysed minerals is shown in Figure 10. Relatively similar REE levels are inferred for the amygdaloidal chlorite mineralization (online Supplementary Fig. S1a, b) and seawater with the exception of MREE where abundances are somewhat higher in the former (Fig. 10). Conversely, the REE patterns of Fe-chlorite and pumpellyite phenocrysts (online Supplementary Fig. S1c, d) are similar to those of black smokers; the REE concentrations are, however, higher in chlorite/pumpellyite by several orders of magnitude (Fig. 10). An inference can be made that in Fe-chlorite and pumpellyite virtually all of the REEs stem from the host rock, while for Mg-rich chlorite amygdules this is not necessarily the case. Research on hydrothermal fluids collected from various geothermal fields shows that the REE balance of percolating fluids increases at higher temperatures (> 230 °C) and when pH decreases (Michard *et al.* 1983), while in low-temperature solutions, the REE content remains low and will not alter regardless of any reasonable fluid/rock ratios (Sanjuan *et al.* 1988). This

https://doi.org/10.1017/S0016756822001030 Published online by Cambridge University Press

means that Mg-chlorite from basaltic amygdules originated from the cold seawater that penetrated down in the recharge zone of the hydrothermal system but did not reach the hot reaction zone (e.g. Valsami & Cann, 1992) or, alternatively, the hydrothermal system was temporarily inactive or cooled down. Such inference is corroborated by the formation temperatures of chlorite (72–100 °C), which fills the amygdules and microveins in rock matrix (vein chlorite, online Supplementary Fig. S2). In the areas of active crustal tectonism, repetitive changes from the active to inactive hydrothermal regime are typical (Moeck, 2014), while periods of activity may be separated by thousands of years of quiescence (Heasler *et al.* 2009). The LREE values shown by amygdaloidal chlorite (online Supplementary Fig. S1a, b) represent a further line of evidence of its low-temperature origin. This illation ensues from a consensus on high-temperature fluids collected from deep-seated hydrothermal areas that are LREE enriched (Klinkhammer *et al.* 1994; Şener *et al.* 2017). Also, the analogue LREE enrichment is documented in hydrothermal chlorite formed from such high-temperature solutions (Tetiker *et al.* 2015). Our line of reasoning therefore advocates a deficiency of LREEs in low-temperature solutions from which chlorite amygdules formed. Should LREEs have been abundant they would, depending upon favourable water/mineral partitioning, be accommodated by nascent chlorite either in its structure or at reactive surfaces (Xiao & Chen, 2020; Tan *et al.* 2021). Since this is not the case, it is reasonable to hypothesize that parental fluid for the formation of chlorite was low-temperature and mildly acidic. In such solutions, REEs are mostly complexed; LREEs are however less complexed than HREEs with the former displaying considerable complexing by Cl^{-}, SO_4^{2-} and CO_3^{2-}, while the latter is commonly complexed by CO_3^{2-} (Valsami & Cann, 1992; Li *et al.* 2019; Gong *et al.* 2021). The abundance of Upper Palaeozoic and Triassic carbonates interlayered with the studied extrusive rocks and tuffs (Goričan *et al.* 2005; Slovenec & Šegvić, 2021) must have contributed to the saturation of the ocean-floor seawater by carbonate ions. These solutions are suggested to have entered ancient hydrothermal systems, interacted with host rocks in the recharge zone, and shortly thereafter produced chlorite amygdules marked by elevated HREE/LREE ratios. This likely explains the characteristic N-MORB-like REE patterns of this type of chlorite (Fig. 10).

REE concentrations of Fe-chlorite (online Supplementary Fig. S1c) and, to a lesser extent, pumpellyite (online Supplementary Fig. S1d) are comparable to those of REE in their extrusive host rocks, which is contrary to the trend exhibited by amygdaloidal chlorite (Fig. 10; D. Smirčić, pers. comm., 2019). SEM images of the former offers an explanation regarding the behaviour of REEs in primary plagioclase (online Supplementary Fig. S1d) and clinopyroxene (online Supplementary Fig. S1e, f), which commonly occur as inclusions in Fe-chlorite. Eroded grain boundaries of mineral inclusions in chlorite are a sign of fluid-facilitated fast chemical reactions that are not in equilibrium with the fluid (e.g. Jamtveit *et al.* 2016). Triassic extrusive rocks of the Western Neotethys affected by hydrothermal activity are largely composed of plagioclase, clinopyroxene, K-feldspar and multiple minor phases (Marci, 1987; Slovenec & Šegvić, 2021). With the exception of plagioclase and clinopyroxene, none of the other phases show any significant REE partitioning (Rollinson & Pease, 2021). Moreover, compared with clinopyroxene, plagioclase is two to three times more abundant in the studied rocks (Marci, 1987) and dissolves preferentially in hydrothermal fluids (Slovenec & Šegvić, 2021). It then follows that in these rocks plagioclase is the main carrier of REEs, and therefore effectively controls the REE content of deep-seated, high-temperature hydrothermal fluids (e.g. Klinkhammer *et al.* 1994; Bau & Dulski, 1999). Several studies have demonstrated remarkable similarities in REE abundances between hydrothermal fluids and plagioclase phenocrysts (Schnetzler & Philpotts, 1970; Papike *et al.* 1996) characterized by the LREE enrichment and a slightly negative Eu anomaly. Both are marked by REE patterns of host extrusive rocks and Fe-chlorite phenocrysts (Fig. 10). A depletion in Yb and Lu in Fe-chlorite is attributed to the strong complexation of REEs by Cl^{2-} in deep-seated acidic hydrothermal fluids, whereby HREEs tend to be less fractionated in hydrothermal precipitates (Flynn & Wayne Burnham, 1978; Allen & Seyfried, 2005). Gadolinium, in contrast, prefers the solid phase (Fig. 10), which corroborates the acidic nature of the percolating fluids (Zielinski & Frey, 1974). An extremely prominent negative anomaly of Ce shown by Fe-chlorite (Fig. 10) reflects the composition of its parental fluid that was sufficiently oxidizing for immobile Ce^{4+} to form, which in turn led to the impoverishment of Ce in the fluid relative to other REE (Sanematsu *et al.* 2011). According to the mechanism proposed by Valsami & Cann (1992), ocean water that enters the hydrothermal recharge zone has to move rapidly and still be oxidizing when attaining high-temperature parts of the system. Since a negative Ce anomaly does not occur in high-temperature hydrothermal pumpellyite, a heterogeneous permeability in the recharge and reaction zone is hypothesized, which gives rise to slow-percolating fluids that are readily reduced prior to the reaction with the rock in which a Ce anomaly is absent (Fig. 10). This line of reasoning is corroborated by the random distribution of sulphides in non-ophiolite basalts/andesites and tuffs (Table 2); specifically, their presence calls for the slower movement of mineralizing fluid, which is followed by temperature decrease leading to dissolution of Fe oxides and eventually sulphide precipitation (e.g. Henley *et al.* 1984).

The REE distribution in phenocrysts of Fe-chlorite is controlled by the temperature, pH, oxidation state, REE complexation by the ligands in the fluid and the fluid/mineral partitioning. Chlorite crystallized from high-temperature solutions will accommodate most of the REE budget of the fluid as a result of the elevated REE distribution coefficients and a relative dominance of chlorite in hydrothermal alteration assemblages (Table 2; Xiao & Chen, 2020; Tan *et al.* 2021).

The REE patterns of pumpellyite phenocrysts are analogous to those of Fe-chlorite (Fig. 10), and therefore a similar origin through a high-temperature hydrothermal dissolution of plagioclase and, to a lesser degree, clinopyroxene is proposed. The absence of a Ce anomaly and depleted values of HREEs are attributed to the heterogeneity of the deep-seated hydrothermal recharge zone where fluids percolated at a different speed, which likely constrained the redox potential. Indeed, the positive Eu anomaly in pumpellyite is characteristic of acidic high-temperature reducing fluids where trivalent Eu is reduced to Eu^{2+} and thus fractionated from the other REEs (e.g. Bau, 1991; Bau & Dulski, 1999).

In summary, the REE distribution in chlorite and pumpellyite of hydrothermal origin can be used as an indicator of the extent and conditions of alteration in fossil hydrothermal systems. We propose a range of hydrothermal solutions that produced amygdaloidal chlorite and phenocrysts of Fe-chlorite and pumpellyite. These phases formed under contrasting temperature conditions and from different solutions, meaning that very distinctive REE patterns resulted (Fig. 10). In the case of chlorite and pumpellyite phenocrysts, minor differences in their REE abundances (Fig. 10)

https://doi.org/10.1017/S0016756822001030 Published online by Cambridge University Press

are attributed to the variations in the redox state and ligand complexation of fluids from which these phenocrysts were derived.

5.c. Geodynamics of the Mesozoic ocean-floor metamorphism in the northwestern segment of Neotethys

The active northwestern continental margin of Palaeotethys, which is composed of non-ophiolitic basaltic (CAB) to acidic rocks and pyroclastites (Fig. 11a), was affected by hydrothermal ocean-floor metamorphism during Middle Triassic time (Anisian–Ladinian; e.g. Lustrino *et al.* 2019). This led to large-scale albitization and chloritization and, to a smaller extent, prehnitization and titanitization of precursor rocks. Geodynamic processes of initial rifting of the northwestern segment of Neotethys, which commenced during late Anisian and early Ladinian time, resulted in outflows of primitive alkaline WPAB and OIB lavas (Fig. 11a; Slovenec *et al.* 2011). Intensive ocean dynamics continued during Late Triassic and Middle Jurassic (Bajocian) time, having transitioned to rapid ocean spreading and formation of E-, T- and N-MORB oceanic lithosphere (Fig. 11b; Slovenec *et al.* 2011). This was subjected to hydrothermal fluxes and seawater (Fig. 9) and gave rise to abundant crystallization of hydrothermal phases under prehnite-actinolite, prehnite-pumpellyite and zeolite facies conditions. Albite, chlorite, prehnite, pumpellyite and titanite are the most abundant hydrothermal phases with minor magnesiohornblende, tremolite, haematite and rare laumontite. The Middle Jurassic vergence transition from extensional to compressional (Bathonian; Fig. 11c) resulted in an intraoceanic convergence and eventually subduction of the oceanic lithosphere, followed by the arc and back-arc IAT and BABB magma generation during Late Jurassic and Early Cretaceous time (Fig. 11d; Slovenec *et al.* 2011). This seems to have created an environment with high rates of water/rock interaction which, in turn, promoted hydrothermal processes in effusive and intrusive basic rocks. Low- to very-low-grade hydrothermal alteration phases resulted in the formation of chlorite, prehnite, pumpellyite, albite and titanite with minor tremolite, epidote, haematite, pyrrhotite, chalcopyrite and pyrite.

6. Conclusions

- Hydrothermal metamorphic processes in Mesozoic ophiolite and non-ophiolite basalts/andesites and tuffs of the active continental margin of the Western Neotethys took place at the ocean floor and, to a lesser degree, during the emplacement of the rocks.
- Major hydrothermal alteration processes that resulted from the fluid–rock interaction include: albitization, chloritization, prehnitization, pumpellyitization, titanitization, epidotization, uralitization and zeolitization. In some locations these processes were limited, leaving relict primary igneous phases.
- Hydrothermal metamorphic parageneses reflect a wide range of temperatures and pressures (from *c.* 450 to < 100 °C and from *c.* 0.4 to < 0.001 GPa) spanning the greenschist facies through to pumpellyite-actinolite and prehnite-pumpellyite to the zeolite facies and diagenesis.
- Initial Sr isotope ratios of the studied rocks show two trends in the intensity of the ocean-floor hydrothermal alteration: (a) during Triassic – Middle Jurassic (Bajocian) time, anorogenic ophiolite rocks (WPAB, E-MORB, T-MORB, N-MORB) formed during extension of oceanic lithosphere, leading to low to medium degrees of alteration, with intensity abating during Middle Triassic – Middle Jurassic (Bajocian) time; and (b) during Middle (Bathonian) to Late Jurassic through Lower Cretaceous time, orogenic ophiolites (IAT, BABB) formed following the establishment of the Neotethyan suprasubduction setting, where there was an apparent increase in the intensity of the hydrothermal alteration of the oceanic lithosphere. During Middle Triassic time, non-ophiolite basalts/andesites and tuffs (CAB) of active continental margin outlined a comparatively broad range of alteration intensities, devoid of any apparent decreasing/increasing alteration trend.
- The chemistry of magmatic host lithologies (i.e. non-ophiolite basalts/andesites and tuffs and ophiolite) dictated the hydrothermal alteration trajectories, leading to the prevalence of quartz and K-bearing phyllosilicates in the former, while the latter is enriched in Ca-silicates (prehnite, pumpellyite and laumontite) and rutile.
- Chlorite, which is a widespread hydrothermal mineral, shows a broad range of compositions that depend on three variables: (a) protolith composition (clinopyroxene versus plagioclase), (b) octahedral/brucite layer cation exchange, and (c) geotectonic affinity of host rocks and rate of hydrothermal alteration. IAT and BABB Upper Jurassic and Lower Cretaceous extrusive and intrusive rocks show the highest degree of chloritization, which is consistent with the Sr isotopic data and petrographic observations that suggest enhanced alteration of clinopyroxene and plagioclase.
- The phase chemistry of pumpellyite is indicative of a continuous decrease in crystallization temperatures at shallower depths of hydrothermal activity.
- Epidote and deuteric amphibole occur almost exclusively in Upper Jurassic/Lower Cretaceous IAT and BABB rocks characterized by a high tectonic activity of the oceanic lithosphere and elevated crystallization temperatures of hydrothermal phases (e.g. chlorite) that belong to the prehnite-pumpellyite and pumpellyite-actinolite facies.
- REEs in chlorite and pumpellyite in Triassic non-ophiolite basalts/andesites and tuffs of active continental margin call for very different hydrothermal solutions to explain their origin. The REE content of these solutions largely stems from the hydrothermal dissolution of plagioclase (and clinopyroxene); once mobilized by hydrothermal fluids, REEs are readily incorporated in newly formed chlorite and pumpellyite. Their variable REE contents are controlled by fluid temperature, composition, redox state and ligand complexation.
- The major and REE geochemistry of critical hydrothermal phases that formed during ocean-floor metamorphism offers important insights into the evolution of the oceanic crust. For the Western Neotethys, where *c.* 150 Ma of hydrothermal history is elucidated starting with Middle Triassic ocean rifting and spreading until Middle Jurassic time, that evolved into Late Jurassic – Early Cretaceous intraoceanic subduction and back-arc extension, ocean-floor metamorphism peaked during the Middle–Late Jurassic intraoceanic subduction. Concurrent intensive tectonism likely facilitated the penetration of seawater into the recharge zone of the hydrothermal system to reach the hot reaction zone. This produced high-temperature bedrock metasomatism at prehnite-pumpellyite and pumpellyite-actinolite facies conditions. The Mesozoic hydrothermal ocean-floor metamorphism occurred prior to the obduction of the ophiolite mélange onto the passive continental margins of Adria during Early Cretaceous time.

https://doi.org/10.1017/S0016756822001030 Published online by Cambridge University Press

Supplementary material. To view supplementary material for this article, please visit https://doi.org/10.1017/S0016756822001030

Acknowledgments. This work was supported by the Croatian Science Foundation (project IP-2019-04-3824) and the Croatian Ministry of Science, Education and Sport (grant no. 181-1951126-1141). Further support was obtained from the Geosciences Clay Laboratory at Texas Tech University. We are especially grateful to Boško Lugović (University of Zagreb) and Hans-Peter Meyer (Universität Heidelberg) for providing excellent microprobe data, as well as Illona Fin (Universität Heidelberg) for preparing high-quality polished thin-sections. We extend our appreciation to Kevin Werts for his guidance in the GeoAnalytical Laboratory at Texas Tech University. We are also indebted to James Browning (Texas Tech University) for his help with sample preparation for LA-ICP-MS analyses. Bruno Tomljenović (University of Zagreb) provided valuable materials needed for the preparation of Figure 1. We also acknowledge Carlos Arbiol (COREM, Québec) for fruitful discussions on chlorite chemistry. Aleksandar Ristić and Kevin Byerly are thanked for assistance with the English language. Critical comments and constructive reviews by Ben Tutolo, Dionysis Foustoukos and Ondrey Nemec as well as editorial assistance by Paul Spry and Tim Johnson have contributed significantly to the manuscript quality.

References

Akaku K, Reed MH, Yagi M, Kai K and Yasuda Y (1991) Chemical and physical processes occurring in the Fushime geothermal system, Kyushu, Japan. *Geochemical Journal* **25**, 315–33.

Allen DE and Seyfried WE (2005) REE controls in ultramafic hosted MOR hydrothermal systems: An experimental study at elevated temperature and pressure. *Geochimica et Cosmochimica Acta* **69**, 675–83.

Alt JC (2009) Very low-grade hydrothermal metamorphism of basic igneous rocks. In *Low-Grade Metamorphism* (eds M Frey and D Robinson), pp. 169–201. New York: John Wiley & Sons, Ltd.

Alt JC and Teagle DAH (2000) Hydrothermal alteration and fluid fluxes in ophiolites and oceanic crust. In *Ophiolites and the Oceanic Crust: New Insights from Field Studies and the Ocean Drilling Program* (eds Y Dilek, EM Moores, D Elthon and A Nicolas), pp. 273–282. Boulder: Geological Society of America.

Aničić B and Jureša M (1984) Basic geological map SFRY 1:100 000. Rogatec sheet. Zagreb: Institut za geološka istraživanja-Savezni geološki zavod Beograd.

Arbiol C, Layne GD, Zanoni G and Šegvić B (2021) Characteristics and genesis of phyllosilicate hydrothermal assemblages from Neoproterozoic epithermal Au-Ag mineralization of the Avalon Zone of Newfoundland, Canada. *Applied Clay Science* **202**, 105960.

Armbruster T, Bonazzi P, Akasaka M, Bermanec V, Chopin C, Gieré R, Heuss-Assbichler S, Liebscher A, Menchetti S, Pan Y and Pasero M (2006) Recommended nomenclature of epidote-group minerals. *European Journal of Mineralogy* **18**, 551–67.

Bastias J, Fuentes F, Aguirre L, Hervé F, Demant A, Deckart K and Torres T (2016) Very low-grade secondary minerals as indicators of palaeo-hydrothermal systems in the Upper Cretaceous volcanic succession of Hannah Point, Livingston Island, Antarctica. *Applied Clay Science* **134**, 246–56.

Bau M (1991) Rare-earth element mobility during hydrothermal and metamorphic fluid-rock interaction and the significance of the oxidation state of europium. *Chemical Geology* **93**, 219–30.

Bau M and Dulski P (1999) Comparing yttrium and rare earths in hydrothermal fluids from the Mid-Atlantic Ridge: implications for Y and REE behaviour during near-vent mixing and for the Y/Ho ratio of Proterozoic seawater. *Chemical Geology* **155**, 77–90.

Berndt ME, Seyfried WE and Janecky DR (1989) Plagioclase and epidote buffering of cation ratios in mid-ocean ridge hydrothermal fluids: Experimental results in and near the supercritical region. *Geochimica et Cosmochimica Acta* **53**, 2283–300.

Bickle MJ and Teagle DAH (1992) Strontium alteration in the Troodos ophiolite: implications for fluid fluxes and geochemical transport in mid-ocean ridge hydrothermal systems. *Earth and Planetary Science Letters* **113**, 219–37.

Boynton WV (1984) *Chapter 3: Cosm*ochemistry of the rare earth elements: meteorite studies. In *Developments in Geochemistry* (ed. P. Henderson), pp. 63–114. Amsterdam: Elsevier.

Brookins DG (1989) Aqueous geochemistry of rare earth elements. *Reviews in Mineralogy and Geochemistry* **21**, 201–25.

Calderón M, Prades CF, Hervé F, Avendaño V, Fanning CM, Massonne HJ, Theye T and Simonetti A (2013) Petrological vestiges of the Late Jurassic-Early Cretaceous transition from rift to back-arc basin in southernmost Chile: New age and geochemical data from the Capitán Aracena, Carlos III, and Tortuga ophiolitic complexes. *Geochemical Journal* **47**, 201–17.

Campbell LS, Charnock J, Dyer A, Hillier S, Chenery S, Stoppa F, Henderson CMB, Walcott R and Rumsey M (2016) Determination of zeolite-group mineral compositions by electron probe microanalysis. *Mineralogical Magazine* **80**, 781–807.

Capuano RM and Cole DR (1982) Fluid-mineral equilibria in a hydrothermal system, Roosevelt hot springs, Utah. *Geochimica et Cosmochimica Acta* **46**, 1353–64.

Coleman RG (1977) *Ophiolites: Ancient Oceanic Lithosphere?* Berlin, Heidelberg: Springer-Verlag.

Coombs DS, Nakamura Y and Vaugnat M (1976) Pumpellyite-actinolite facies schist of the Taveyanne formation near Loeche, Valais, Switzerland. *Journal of Petrology* **17**, 440–47.

Deer WA FRS, Howie RA and Zussman J (2013) *An Introduction to the Rock-Forming Minerals*, 3rd edition. London: Mineralogical Society of Great Britain and Ireland.

Enami M, Suzuki K, Liou JG and Bird DK (1993) Al-Fe3+ and F-OH substitutions in titanite and constraints on their P-T dependence. *European Journal of Mineralogy* **5**, 219–32.

Flynn RT and Wayne Burnham C (1978) An experimental determination of rare earth partition coefficients between a chloride containing vapor phase and silicate melts. *Geochimica et Cosmochimica Acta* **42**, 685–701.

Fouquet Y, Pelleter E, Konn C, Chazot G, Dupré S, Alix AS, Chéron S, Donval JP, Guyader V, Etoubleau J, Charlou JL, Labanieh S and Scalabrin C (2018) Volcanic and hydrothermal processes in submarine calderas: the Kulo Lasi example (SW Pacific). *Ore Geology Reviews* **99**, 314–43.

Fujibayashi N, Asakura K, Hattori T and Allen S (2014) Pillow lava and spasmodic submarine fire fountaining in the middle Miocene marginal basin, Sado Island, Japan. *Island Arc* **23**, 344–64.

Fyfe W and Lonsdale P (1981) Ocean floor hydrothermal activity. *The Sea* **7**, 589–638.

German CR and Lin J (2004) The thermal structure of the oceanic crust, ridge-spreading and hydrothermal circulation: How well do we understand their inter-connections? *Geophysical Monograph Series* **148**, 1–18.

Gillis KM, Coogan LA and Pedersen R (2005) Strontium isotope constraints on fluid flow in the upper oceanic crust at the East Pacific Rise. *Earth and Planetary Science Letters* **232**, 83–94.

Girardeau J and Mevel C (1982) Amphibolitized sheared gabbros from ophiolites as indicators of the evolution of the oceanic crust: Bay of Islands, Newfoundland. *Earth and Planetary Science Letters* **61**, 151–65.

Gong Q, Li F, Lu C, Wang H and Tang H (2021) Tracing seawater- and terrestrial-sourced REE signatures in detritally contaminated, diagenetically altered carbonate rocks. *Chemical Geology* **570**, 120169.

Goričan Š, Halamić J, Grgasović T and Kolar-Jurkovšek T (2005) Stratigraphic evolution of Triassic arc-backarc system in northwestern Croatia. *Bulletin de la Société Géologique de France* **176**, 3–22.

Haas J, Mioč P, Pamić J, Tomljenović B, Árkai P, Bérczi-Makk A, Koroknai B, Kovács S and Rálisch-Felgenhauer E (2000) Complex structural pattern of the Alpine–Dinaridic–Pannonian triple junction. *International Journal of Earth Sciences* **89**, 377–89.

Harlov DE and Marschall HR (2009) Mechanisms of metasomatic reactions. *Mineralogy and Petrology* **95**, 159–61.

Hawthorne FC, Oberti R, Harlow GE, Maresch WV, Martin RF, Schumacher JC and Welch MD (2012) Nomenclature of the amphibole supergroup. *American Mineralogist* **97**, 2031–48.

Heasler HP, Jaworowski C and Foley D (2009) Geothermal systems and monitoring hydrothermal features. In *Geological Monitoring* (eds R Young and L Norby), pp. 105–40. Boulder, CO: Geological Society of America.

Henley RW, Truesdell AH, Barton PB Jr and Whitney JA (1984) *Fluid-Mineral Equilibria in Hydrothermal Systems*. Littleton: Society of Economic Geologists.

Høgdahl OT, Melsom S and Bowen VT (1968) Neutron activation analysis of lanthanide elements in sea water. In *Trace Inorganics in Water* (ed. RA Baker), pp. 308–25. New York: American Chemical Society, Advances in Chemistry 73.

Ilijima A and Utada M (1972) Zeolitic zoning of the Neogene pyroclastic rocks in Japan. *Japanese Journal of Geology and Geography* **42**, 61–83.

Inoue A and Utada M (1991) Smectite-to-chlorite transformation in thermally metamorphosed volcanoclastic rocks in the Kamikita area, northern Honshu, Japan. *American Mineralogist* **76**, 628–40.

Inoue A, Inoué S and Utada M (2018) Application of chlorite thermometry to estimation of formation temperature and redox conditions. *Clay Minerals* **53**, 143–58.

Ishizuka H (1991) Pumpellyite from zeolite facies metabasites of the Horokanai ophiolite in the Kamuikotan zone, Hokkaido, Japan. *Contributions to Mineralogy and Petrology* **107**, 1–7.

Jamtveit B, Austrheim H, Putnis A (2016) Disequilibrium metamorphism of stressed lithosphere. *Earth-Science Reviews* **154**, 1–13.

Jochum KP, Willbold M, Raczek I, Stoll B and Herwig K (2005) Chemical characterisation of the USGS reference glasses GSA-1G, GSC-1G, GSD-1G, GSE-1G, BCR-2G, BHVO-2G and BIR-1G using EPMA, ID-TIMS, ID-ICP-MS and LA-ICP-MS. *Geostandards and Geoanalytical Research* **29**, 285–302.

Judik K, Árkai P, Horváth P, Dobosi G and Al A (2005) Diagenesis and low-temperature metamorphism of Mt. Medvednica, Croatia: Mineral assemblages and phyllosilicate characteristics. *Acta Geologica Hungarica* **47**, 151–76.

Kamimura K, Hirajima T and Fujimoto Y (2012) Finding of prehnite-pumpellyite facies metabasites from the Kurosegawa belt in Yatsushiro area, Kyushu, Japan. *Journal of Mineralogical and Petrological Sciences* **107**, 99–104.

Klinkhammer GP, Elderfield H, Edmond JM and Mitra A (1994) Geochemical implications of rare earth element patterns in hydrothermal fluids from mid-ocean ridges. *Geochimica et Cosmochimica Acta* **58**, 5105–13.

Kovács Z, Demangel I, Richoz S, Hippler D, Baldermann A and Krystyn L (2020) New constraints on the evolution of 87Sr/86Sr of seawater during the Upper Triassic. *Global and Planetary Change* **192**, 103255.

Kranidiotis P and MacLean WH (1987) Systematics of chlorite alteration at the Phelps Dodge massive sulfide deposit, Matagami, Québec. *Economic Geology* **82**, 1898–911.

Kretz R (1983) Symbols for rock-forming minerals. *American Mineralogist* **68**, 277–79.

Kuhn T, Versteegh GJM, Villinger H, Dohrmann I, Heller C, Koschinsky A, Kaul N, Ritter S, Wegorzewski AV and Kasten S (2017) Widespread seawater circulation in 18–22 Ma oceanic crust: Impact on heat flow and sediment geochemistry. *Geology* **45**, 799–802.

Li F, Webb GE, Algeo TJ., Kershaw S, Lu C, Oehlert AM, Gong Q, Pourmand A and Tan X (2019) Modern carbonate ooids preserve ambient aqueous REE signatures. *Chemical Geology* **509**, 163–77.

Liou JG, Maruyama S and Cho M (1985) Phase equilibria and mixed parageneses of metabasites in low-grade metamorphism. *Mineralogical Magazine* **49**, 321–33.

Lowell RP, Farough A, Hoover J and Cummings K (2013) Characteristics of magma-driven hydrothermal systems at oceanic spreading centers. *Geochemistry, Geophysics, Geosystems* **14**, 1756–70.

Lugović B, Slovenec D, Schuster R, Schwarz WH and Horvat M (2015) Petrology, geochemistry and tectono-magmatic affinity of gabbroic olistoliths from the ophiolite mélange in the NW Dinaric-Vardar ophiolite zone (Mts. Kalnik and Ivanščica, North Croatia). *Geologia Croatica* **68**, 25–49.

Lustrino M, Abbas H, Agostini S, Gaggiati M, Carminati E and Gianolla P (2019) Origin of Triassic magmatism of the Southern Alps (Italy): constraints from geochemistry and Sr-Nd-Pb isotopic ratios. *Gondwana Research* **75**, 218–38.

Marci V (1987) Mineral assemblages in amygdales of volcanic rocks from Ivanščica. *Geološki vjesnik* **40**, 131–8.

Mével C (2003) Serpentinization of abyssal peridotites at mid-ocean ridges. *Comptes Rendus Geoscience* **335**, 825–52.

Michard A and Albarède F (1986) The REE content of some hydrothermal fluids. *Chemical Geology* **55**, 51–60.

Michard A, Albarède F, Michard G, Minster JF and Charlou JL (1983) Rare-earth elements and uranium in high-temperature solutions from East Pacific Rise hydrothermal vent field (13 °N). *Nature* **303**, 795–97.

Moeck IS (2014) Catalog of geothermal play types based on geologic controls. *Renewable and Sustainable Energy Reviews* **37**, 867–82.

Morad S, El-Ghali M, Caja MA, Sirat M, Al-Ramadan K and Mansurbeg H (2010) Hydrothermal alteration of plagioclase in granitic rocks from Proterozoic basement of SE Sweden. *Geological Journal* **45**, 105–16.

Mottl MJ (1983) Metabasalts, axial hot springs, and the structure of hydrothermal systems at mid-ocean ridges (Atlantic Ocean). *Geological Society of America Bulletin* **94**, 161–80.

Mottl MJ and McConachy TF (1990) Chemical processes in buoyant hydrothermal plumes on the East Pacific Rise near 21°N. *Geochimica et Cosmochimica Acta* **54**, 1911–27.

Pamić J (1984) Triassic magmatism of the Dinarides in Yugoslavia. *Tectonophysics* **109**, 273–307.

Pamić J and Tomljenović B (1998) Basic geological data from the Croatian part of the Zagorje - Mid-Transdanubian Zone. *Acta Geologica Hungarica* **41**, 389–400.

Paoli G, Dini A, Petrelli M and Rocchi S (2019) HFSE-REE transfer mechanisms during metasomatism of a late Miocene peraluminous granite intruding a carbonate host (Campiglia Marittima, Tuscany). *Minerals* **9**, 682.

Papike JJ, Fowler GW, Shearer CK and Layne GD (1996) Ion microprobe investigation of plagioclase and orthopyroxene from lunar Mg-suite norites: Implications for calculating parental melt REE concentrations and for assessing postcrystallization REE redistribution. *Geochimica et Cosmochimica Acta* **60**, 3967–78.

Peucker-Ehrenbrink B and Fiske GJ (2019) A continental perspective of the seawater 87Sr/86Sr record: A review. *Chemical Geology* **510**, 140–65.

Pletničar M, Premru U and Herak M (1975) Basic geological map of SFRY 1:100.000. Sheet Novo Mesto. Ljubljana: Geološki zavod Ljubljana-Savezni geološki zavod Beograd.

Pouchou JL and Pichoir F (1984) A new model for quantitative analyses. I. Application to the analysis of homogeneous samples. *La Recherche Aérospatiale* **3**, 13–38.

Rahn M, Mullis J, Erdelbrock K and Frey M (1994) Very low-grade metamorphism of the Taveyanne greywacke, Glarus Alps, Switzerland. *Journal of Metamorphic Geology* **12**, 625–41.

Ray D, Mevel C and Banerjee R (2009) Hydrothermal alteration studies of gabbros from Northern Central Indian Ridge and their geodynamic implications. *Journal of Earth System Science* **118**, 659.

Rollinson H and Pease V (2021) *Using Geochemical Data: To Understand Geological Processes*. Cambridge: Cambridge University Press.

Rottier B, Kouzmanov K, Wälle M, Bendezú R and Fontboté L (2016) Sulfide replacement processes revealed by textural and LA-ICP-MS trace element analyses: Example from the early mineralization stages at Cerro de Pasco, Peru. *Economic Geology* **111**, 1347–67.

Saccani E and Tassinari R (2015) The role of MORB and SSZ magma-types in the formation of Jurassic ultramafic cumulates in the Mirdita ophiolites (Albania) as deduced from chromian spinel and olivine chemistry. *Ofioliti* **40**, 37–56.

Sanematsu K, Moriyama T, Sotouky L and Watanabe Y (2011) Mobility of rare earth elements in basalt-derived laterite at the Bolaven Plateau, Southern Laos. *Resource Geology* **61**, 140–58.

Sanjuan B, Michard A and Michard G (1988) Influence of the temperature of CO2-rich springs on their aluminium and rare-earth element contents. *Chemical Geology* **68**, 57–67.

Scambelluri M, Rampone E and Piccardo GB (2001) Fluid and element cycling in subducted serpentinite: A trace-element study of the Erro-Tobbio

https://doi.org/10.1017/S0016756822001030 Published online by Cambridge University Press

high-pressure ultramafites (Western Alps, NW Italy). *Journal of Petrology* **42**, 55–67.

Schiffman P and Liou JG (1983) Synthesis of Fe-pumpellyite and its stability relations with epidote. *Journal of Metamorphic Geology* **1**, 91–101.

Schiffman P and Staudigel H (1994) Hydrothermal alteration of a seamount complex on La Palma, Canary Islands: Implications for metamorphism in accreted terranes. *Geology* **22**, 151–54.

Schmid SM, Bernoulli D, Fügenschuh B, Matenco L, Schefer S, Schuster R, Tischler M and Ustaszewski K (2008) The Alpine-Carpathian-Dinaridic orogenic system: correlation and evolution of tectonic units. *Swiss Journal of Geosciences* **101**, 139–83.

Schmid SM, Fügenschuh B, Kounov A, Maţenco L, Nievergelt P, Oberhänsli R, Pleuger J, Schefer S, Schuster R, Tomljenović B, Ustaszewski K and van Hinsbergen DJJ (2020) Tectonic units of the Alpine collision zone between Eastern Alps and western Turkey. *Gondwana Research* **78**, 308–74.

Schnetzler CC and Philpotts JA (1970) Partition coefficients of rare-earth elements between igneous matrix material and rock-forming mineral phenocrysts—II. *Geochimica et Cosmochimica Acta* **34**, 331–40.

Šegvić B, Kukoč D, Dragičević I, Vranjković A, Brčić V, Goričan Š, Babajić E and Hrvatović H (2014) New record of Middle Jurassic radiolarians and evidence of Neotethyan dynamics documented in a mélange from the Central Dinaridic Ophiolite Belt (CDOB, NE Bosnia and Herzegovina). *Ofioliti* **39**, 33–43.

Šegvić B, Lugović B, Slovenec D and Meyer H-P (2016) Mineralogy, petrology and geochemistry of amphibolites from the Kalnik Mt. (Sava Unit, North Croatia): Implications for the evolution of north-westernmost part of the Dinaric-Vardar branch of Mesozoic Tethys. *Ofioliti* **41**, 35–58.

Šegvić B, Zanoni G and Moscariello A (2020) On the origins of eogenetic chlorite in verdine facies sedimentary rocks from the Gabon Basin in West Africa. *Marine and Petroleum Geology* **112**, 104064.

Şener MF, Şener M and Uysal IT (2017) The evolution of the Cappadocia Geothermal Province, Anatolia (Turkey): geochemical and geochronological evidence. *Hydrogeology Journal* **25**, 2323–45.

Seyfried WE and Bischoff JL (1981) Experimental seawater-basalt interaction at 300°C, 500 bars, chemical exchange, secondary mineral formation and implications for the transport of heavy metals. *Geochimica et Cosmochimica Acta* **45**, 135–47.

Šikić K, Basch O and Šimunić An (1977) Basic geological map of SFRY 1:100.000. Sheet Zagreb. Zagreb: Institut za geološka istraživanja-Savezni geološki zavod Beograd.

Šimunić An, Pikija M and Hećimović I (1982) Basic geological map of SFRY 1:100.000. Sheet Varaždin. Zagreb: Institut za geološka istraživanja-Savezni geološki zavod Beograd.

Slovenec D, Lugović B, Meyer H-P and Šiftar GG (2011) A tectono-magmatic correlation of basaltic rocks from ophiolite mélanges at the north-eastern tip of the Sava-Vardar suture zone, northern Croatia, constrained by geochemistry and petrology. *Ofioliti* **36**, 77–100.

Slovenec D, Lugović B and Slovenec D (2012) Sekundarne mineralne parageneze u mafitnim ekstruzivnim stijenama iz ofiolitnog melanža Medvednice (Hrvatska). [Secondary mineral paragenesis in the mafic extrusive rocks from the Mt. Medvednica ophiolite melange (Croatia).] *Rudarsko-Geološko-Naftni Zbornik* **25**, 33–46 [in Croatian with English abstract].

Slovenec D and Šegvić B (2018) Boninite volcanic rocks from the mélange of NW Dinaric-Vardar ophiolite zone (Mt. Medvednica, Croatia) – record of Middle to Late Jurassic arc-forearc system in the Tethyan subduction factory. *Mineralogy and Petrology* **113**, 17–37.

Slovenec D and Šegvić B (2021) Middle Triassic high-K calc-alkaline effusive and pyroclastic rocks from the Zagorje-mid-Transdanubian zone (Mt. Kuna Gora; NW Croatia): mineralogy, petrology, geochemistry and tectonomagmatic affinity. *Geologica Acta* **19**, 1–23.

Smirčić D, Kolar-Jurkovšek T, Aljinović D, Barudžija U, Jurkovšek B and Hrvatović H (2018) Stratigraphic definition and correlation of Middle Triassic volcaniclastic facies in the external Dinarides: Croatia and Bosnia and Herzegovina. *Journal of Earth Science* **29**, 864–78.

Sun SC, Zhang L, Li RH, Hao TW, Wang JY, Li ZQ, Zhang F, Zhang XJ and Guo H (2019) Process and mechanism of gold mineralization at the Zhengchong Gold Deposit, Jiangnan Orogenic Belt: evidence from the arsenopyrite and chlorite mineral thermometers. *Minerals*, **9**, 133.

Tan W, Mao Q, Yu M, Sun Y and Lv X (2021) Mineralization of the Tuwu Porphyry Cu deposit in eastern Tianshan, NW China: insights from in situ trace elements of chlorite and pyrite. *Frontiers in Earth Science* **9**, 413.

Tetiker S, Yalçın H and Bozkaya Ö (2015) Approaches to the low-grade metamorphic history of the Karakaya complex by chlorite mineralogy and geochemistry. *Minerals* **5**, 221–46.

Tillick DA, Peacor DR and Mauk JL (2001) Genesis of dioctahedral phyllosilicates during hydrothermal alteration of volcanic rocks: I. The Golden Cross epithermal ore deposit, New Zealand. *Clays and Clay Minerals* **49**, 126–40.

Valsami E and Cann JR (1992) Mobility of rare earth elements in zones of intense hydrothermal alteration in the Pindos ophiolite, Greece. In *Ophiolites and their Modern Ocean Analogues* (eds LM Parson, BJ Murton and P Browning), pp. 219–32. Geological Society of London, Special Publication no. **60**.

Vlahović I, Tišljar J, Velić I and Matičec D (2005) Evolution of the Adriatic Carbonate Platform: Palaeogeography, main events and depositional dynamics. *Palaeogeography, Palaeoclimatology, Palaeoecology* **220**, 333–60.

Von Damm KL, Edmond JM, Grant B, Measures CI, Walden B and Weiss RF (1985) Chemistry of submarine hydrothermal solutions at 21 °N, East Pacific Rise. *Geochimica et Cosmochimica Acta* **49**, 2197–220.

Wang Y, Lin M, Xi K, Cao Y, Wang J, Yuan G, Kashif M and Song M (2018) Characteristics and origin of the major authigenic minerals and their impacts on reservoir quality in the Permian Wutonggou Formation of Fukang Sag, Junggar Basin, western China. *Marine and Petroleum Geology* **97**, 241–59.

Wilson DS, Teagle DAH, Alt JC, Banerjee NR, Umino S, Miyashita S, Acton GD, Anma R, Barr SR, Belghoul A, Carlut J, Christie DM, Coggon RM, Cooper KM, Cordier C, Crispini L, Durand SR, Einaudi F, Galli L, Gao Y, Geldmacher J, Gilbert LA, Hayman NW, Herrero-Bervera E, Hirano N, Holter S, Ingle S, Jiang S, Kalberkamp U, Kerneklian M, Koepke J, Laverne C, Vasquez HLL, Maclennan J, Morgan S, Neo N, Nichols HJ, Park S.-H, Reichow MK, Sakuyama T, Sano T, Sandwell R, Scheibner B, Smith-Duque CE, Swift SA, Tartarotti P, Tikku AA, Tominaga M, Veloso EA, Yamasaki T, Yamazaki S and Ziegler C (2006) Drilling to gabbro in intact ocean crust. *Science* **312**, 1016–20.

Xiao B and Chen H (2020) Elemental behavior during chlorite alteration: New insights from a combined EMPA and LA-ICP-MS study in porphyry Cu systems. *Chemical Geology* **543**, 119604.

Zane A and Weiss Z (1998) A procedure for classifying rock-forming chlorites based on microprobe data. *Rendiconti Lincei* **9**, 51–6.

Zielinski RA and Frey FA (1974) An experimental study of the partitioning of a rare earth element (Gd) in the system diopside—aqueous vapour. *Geochimica et Cosmochimica Acta* **38**, 545–65.